

Angular momentum and topology in semiconducting single-wall carbon nanotubes

W. Izumida,^{1,*} R. Okuyama,^{1,†} A. Yamakage,^{2,3,‡} and R. Saito¹

¹*Department of Physics, Tohoku University, Sendai 980-8578, Japan*

²*Department of Applied Physics, Nagoya University, Nagoya 464-8603, Japan*

³*Institute for Advanced Research, Nagoya University, Nagoya 464-8601, Japan*
(Dated:)

Semiconducting single-wall carbon nanotubes are classified into two types by means of orbital angular momentum of valley state, which is useful to study their low energy electronic properties in finite-length. The classification is given by an integer d , which is the greatest common divisor of two integers n and m specifying the chirality of nanotubes, by analyzing cutting lines. For the case that d is equal to or greater than four, two lowest subbands from two valleys have different angular momenta with respect to the nanotube axis. Reflecting the decoupling of two valleys, discrete energy levels in finite-length nanotubes exhibit nearly fourfold degeneracy and its small lift by the spin-orbit interaction. For the case that d is less than or equal to two, in which two lowest subbands from two valleys have the same angular momentum, discrete levels exhibit lift of fourfold degeneracy reflecting the coupling of two valleys. Especially, two valleys are strongly coupled when the chirality is close to the armchair chirality. An effective one-dimensional lattice model is derived by extracting states with relevant angular momentum, which reveals the valley coupling in the eigenstates. A bulk-edge correspondence, relationship between number of edge states and the winding number calculated in the corresponding bulk system, is analytically shown by using the argument principle, which enables us to estimate the number of edge states from the bulk property. The number of edge states depends not only on the chirality but also on the shape of boundary.

PACS numbers: 73.63.Fg, 73.22.Dj

I. INTRODUCTION

Recent studies of quantum transport have revealed that single-wall carbon nanotubes (SWNTs) contain richer phenomena, especially in terms of the spin and valley degrees of freedom.¹ Fourfold degeneracy of SWNTs, observed in the tunneling spectroscopy,^{2–11} has been widely considered as an intrinsic property of SWNTs, reflecting the two degenerate K and K' valleys in the two-dimensional (2D) Brillouin zone (BZ), together with two spin states of up and down. Measurements for ultra-clean SWNTs^{12–15} show fine structures of lift of fourfold degeneracy caused by the spin-orbit interaction.^{16–21} Recent studies focused on the angular momenta of two valleys as a conserved quantity in disorder-free finite-length metallic SWNTs (m-SWNTs).^{22,23} It is shown that the two valleys have the same angular momentum for the so-called metal-2 nanotubes, whereas they have different angular momenta for the metal-1 nanotubes.^{22,24} (The definitions of metal-1 and metal-2 are given in Sec. II.) For finite-length m-SWNTs which has the same rotational symmetry with the bulk, the two valleys are decoupled and the spin-orbit interaction lifts the fourfold degeneracy for the metal-1 nanotubes, whereas valley coupling due to the inter-valley scattering at the ends lifts the fourfold degeneracy, regardless of spin-orbit interaction, for the metal-2 nanotubes.^{22,23} Valley coupling could play a role for large lift of the fourfold degeneracy in the experiments.^{7,9–11,15,25,26}

Many of the quantum transport measurements have been performed for the m-SWNTs,^{1–15} which could contain narrow energy gap induced by curvature of nanotube

surface. Conducting of the semiconducting SWNTs (s-SWNTs) has also been investigated by adjusting the gate voltage.^{1,8,27,28} In fact, the s-SWNTs are double abundant of the m-SWNTs.²⁹ However, the relationship between valley, angular momentum, and the finite-length effect is not well analyzed for the s-SWNTs, even though they play essential roles in the quantum transport measurements. Here we will focus on the s-SWNTs.

In this paper, we will classify the s-SWNTs by means of the angular momentum of the valley. We will show that the classification is performed by an integer $d = \text{gcd}(n, m)$, which is the greatest common divisor (gcd) of n and m , where the integer set (n, m) specifies the chiral vector.²⁹ (See Sec. II for the definition of chiral vector.) For the s-SWNTs with $d \geq 4$, the two valleys have different angular momenta and the two valleys are decoupled. For this case the spin-orbit interaction lifts the fourfold degeneracy in the finite-length nanotubes, as in the case of metal-1 nanotubes.²² On the other hand, for the s-SWNTs with $d = 1$ and $d = 2$, the two valleys have the same angular momentum and valley coupling lifts the fourfold degeneracy, as in the case of metal-2 nanotubes.²² Especially for the case of $|n - m| = 2$, which is close to the armchair chirality, the two valleys are strongly coupled. Note that $d = 3$, more generally $\text{mod}(d, 3) = 0$, holds only for a part of m-SWNTs. In order to understand the coupling of two valleys, an effective one-dimensional (1D) lattice model is derived and analyzed. Chirality and edge shape dependences of the number of edge states, as another intrinsic feature in the finite-length nanotubes, are given by expanding the theory for valley coupling. Especially, a bulk-edge correspondence, relationship between the number of edge

states and the winding number given in the corresponding bulk system, is analytically shown.

The present study reveals that the coupling of two valleys occurs in the majority of SWNTs, *even for ultra-clean tubes with clean edges*, which conserve the angular momentum of ideal bulk states of electrons. The valley coupling appears as the lift of fourfold degeneracy, regardless of the spin-orbit interaction. Moreover, the bulk-edge correspondence for edge states in the semiconducting energy gap reveals another feature of SWNTs as topological insulating materials.

This paper is organized as follows. In Sec. II, classification of the s-SWNTs by means of the angular momentum of the valley is given. In Sec. III, numerical calculation is given for finite-length s-SWNTs, which shows the valley coupling for $d \leq 2$ cases. In Sec. IV, an effective 1D lattice model is derived (Sec. IV A), eigenstates under boundary is analyzed (Sec. IV B), and number of edge states is given from both a mode analysis of boundary condition and a topological viewpoint for the bulk 1D lattice model (Sec. IV C). The conclusion is given in Sec. V.

II. ANGULAR MOMENTA OF TWO VALLEYS

In order to discuss the angular momentum of SWNTs, we first redefine the previous concept of cutting line,³⁰ by using the helical-angular construction.³¹

Let us consider a SWNT defined by rolling up the graphene sheet in the direction of the chiral vector $\mathbf{C}_h = n\mathbf{a}_1 + m\mathbf{a}_2 \equiv (n, m)$, where n and m are integers specifying the chirality of SWNT, $\mathbf{a}_1 = (\sqrt{3}/2, 1/2)a$ and $\mathbf{a}_2 = (\sqrt{3}/2, -1/2)a$ are the unit vectors of graphene, $a = 0.246$ nm is the lattice constant.²⁹ In this paper, we consider the rolling of the graphene from the front to the back, and, unless otherwise indicated, the case of $n \geq m \geq 0$, which correspond to the “zigzag-right handedness”, except for the zigzag ($m = 0$) and armchair ($n = m$) nanotubes, according to Ref. 32. The nanotubes of opposite handedness, zigzag-left handedness, are given for (m, n) , or rolling of the graphene sheet from the back to the front.³²

A. Cutting line

Here we introduce the cutting line defined under the helical-angular construction,³¹ and show the angular momentum of K and K' points for the m-SWNTs,²² which are known in the previous studies.

To discuss the angular momenta of two valleys, it is convenient to introduce an alternative set of unit vectors, utilizing the rotational and the helical symmetry of SWNT, \mathbf{C}_h/d and $\mathbf{R} = p\mathbf{a}_1 + q\mathbf{a}_2$.^{33,34} Here $d = \text{gcd}(n, m)$ is the greatest common divisor (gcd) of n and m , and the integers p and q are chosen to satisfy

the relation of

$$mp - nq = d. \quad (1)$$

Translation with \mathbf{C}_h/d corresponds to the \mathcal{C}_d rotation with respect to the nanotube axis. The vector \mathbf{R} has a_z and $\Delta\theta d_t/2$ components in the axis and circumference directions, respectively, where

$$a_z = \frac{Td}{N} \quad (2)$$

is the shortest distance between two A (B) atoms in the axis direction, $T = a\sqrt{3(n^2 + m^2 + nm)}/d_R$ is the lattice constant of the 1D nanotube, $N = 2(n^2 + m^2 + nm)/d_R$ is the number of A (B) atoms in the 1D nanotube unit cell, $d_R = \text{gcd}(2n + m, 2m + n)$,

$$\Delta\theta = 2\pi \frac{t_1 q - t_2 p}{N} \quad (3)$$

is the azimuth component of \mathbf{R} in the cylindrical coordinates, $d_t = |\mathbf{C}_h|/\pi$ is the diameter of nanotube, $t_1 = (2m + n)/d_R$, $t_2 = -(2n + m)/d_R$. There is an arbitrariness to define p and q since $\mathbf{R} + \alpha\mathbf{C}_h/d$ also satisfies the definition of \mathbf{R} , with $\alpha = 0, 1, \dots, d-1$. Two reciprocal lattice vectors, which are conjugate to \mathbf{C}_h/d and \mathbf{R} , are given by

$$\mathbf{Q}_1 = -q\mathbf{b}_1 + p\mathbf{b}_2, \quad \mathbf{Q}_2 = \frac{m}{d}\mathbf{b}_1 - \frac{n}{d}\mathbf{b}_2, \quad (4)$$

where $\mathbf{b}_1 = (2\pi/a)(1/\sqrt{3}, 1)$ and $\mathbf{b}_2 = (2\pi/a)(1/\sqrt{3}, -1)$ are the reciprocal lattice vectors of graphene, and the relations $\mathbf{Q}_1 \cdot \mathbf{C}_h/d = \mathbf{Q}_2 \cdot \mathbf{R} = 2\pi$, $\mathbf{Q}_1 \cdot \mathbf{R} = \mathbf{Q}_2 \cdot \mathbf{C}_h/d = 0$ hold. The wavevector in the first BZ is expressed by

$$\mathbf{k} = \mu \frac{\mathbf{Q}_1}{d} + k \frac{\mathbf{Q}_2}{|\mathbf{Q}_2|}, \quad (5)$$

with

$$\mu = 0, 1, \dots, d-1, \quad \text{and} \quad 0 \leq k < \frac{2\pi}{a_z}. \quad (6)$$

Note that $|\mathbf{Q}_2| = 2\pi/a_z$. The discretization of μ is due to the periodic boundary condition in the circumference direction, which requires $\mathbf{k} \cdot \mathbf{C}_h/2\pi$ is an arbitrary integer. The integer μ is the orbital angular momentum around the nanotube axis, and each line in the 2D k -space specified by μ is called cutting line.

In comparison to the conventional formulation,²⁹ we have the relations, $\mathbf{K}_1 = \mathbf{Q}_1/d + \mathbf{Q}_2\Delta\theta/2\pi$ and $\mathbf{K}_2 = \mathbf{Q}_2d/N$, where \mathbf{K}_1 represents the separation of cutting lines and \mathbf{K}_2 is the vector of short cutting lines in the conventional formulation, and they are orthogonal each other. The cutting lines in the conventional formulation are given by $\mu\mathbf{K}_1 + k\mathbf{K}_2/|\mathbf{K}_2|$ with $\mu = 0, \dots, N-1$ and $-\pi/T \leq k < \pi/T$. The present formulation of 2D BZ by Eq. (5) is essentially the same with that given in our previous study,²² in which the rectangular shape of 2D BZ is given by the translation of the triangle at the

corner of the present parallelogram shape of 2D BZ by $(d\Delta\theta/2\pi)\mathbf{Q}_2$. It is convenient to use the two reciprocal lattice vectors \mathbf{Q}_1 and \mathbf{Q}_2 in the present formulation, rather than \mathbf{K}_1 and \mathbf{K}_2 , to specify not only the angular momenta of two valleys,²² but also the closest positions of K and K' points on the cutting lines, as shown below.

In general, a K point, $\overrightarrow{\Gamma K} = (2\mathbf{b}_1 + \mathbf{b}_2)/3$, is expressed by,

$$\overrightarrow{\Gamma K} = \frac{2n+m}{3} \frac{\mathbf{Q}_1}{d} + \frac{2p+q}{3} \mathbf{Q}_2. \quad (7)$$

A K' point is specified by $\overrightarrow{\Gamma K'} = -\overrightarrow{\Gamma K}$. By comparing Eqs. (5) and (7), it is concluded that the SWNT is metallic when $\text{mod}(2n+m, 3) = 0$,²⁹ because the cutting lines with $(2n+m)/3$ and $-(2n+m)/3$, or equivalently,

$$\mu_K = \text{mod} \left(\frac{2n+m}{3}, d \right), \quad (8)$$

$$\mu_{K'} = \text{mod} \left(-\frac{2n+m}{3}, d \right), \quad (9)$$

where $0 \leq \mu_K, \mu_{K'} \leq d-1$, pass through the K and K' points, respectively, whereas it is semiconducting when $\text{mod}(2n+m, 3) \neq 0$ because there is no cutting line which passes the K or K' points. Here we used the property that the cutting line of μ is equivalent to that of $\text{mod}(\mu, d)$. Further, the m-SWNTs are classified into metal-1 ($d_R = d$) and metal-2 ($d_R = 3d$).²⁹ Two different cutting lines $\mu_K \neq 0$ and $\mu_{K'} \neq 0$ pass through K and K' points, respectively, for metal-1, while, the cutting line $\mu_K = \mu_{K'} = 0$ passes through both K and K' points for metal-2, as already proven in Ref. 22. The K (K') point on the line μ_K ($\mu_{K'}$) is given by

$$k_K = \frac{2\pi}{3a_z} \text{mod}(2p+q, 3), \quad (10)$$

$$k_{K'} = \frac{2\pi}{3a_z} \text{mod}(-2p-q, 3). \quad (11)$$

Especially for the metal-2 nanotubes, since the relation $\text{mod}(2p+q, 3) = \text{mod}(2m/d, 3)$ holds, $k_K = 4\pi/3a_z$ ($2\pi/3a_z$) and $k_{K'} = 2\pi/3a_z$ ($4\pi/3a_z$) for $\text{mod}(m/d, 3) = 1$ (2), as shown in Ref. 22.

B. Classification of s-SWNTs

Using the new definition we classify the s-SWNTs. For the s-SWNTs, the point closest to the K point on the cutting lines is given by,

$$\overrightarrow{\Gamma K} \mp \frac{\mathbf{K}_1}{3} = \frac{2n+m \mp 1}{3} \frac{\mathbf{Q}_1}{d} + \frac{2p+q \mp \frac{\Delta\theta}{2\pi}}{3} \mathbf{Q}_2, \quad (12)$$

where $-$ and $+$ are applied for type-1 [$\text{mod}(2n+m, 3) = 1$] and type-2 [$\text{mod}(2n+m, 3) = 2$] s-SWNTs,³⁵ respectively (see Fig. 1). Here, we define μ specifying a cutting line which passes through a point closest to a K (K')

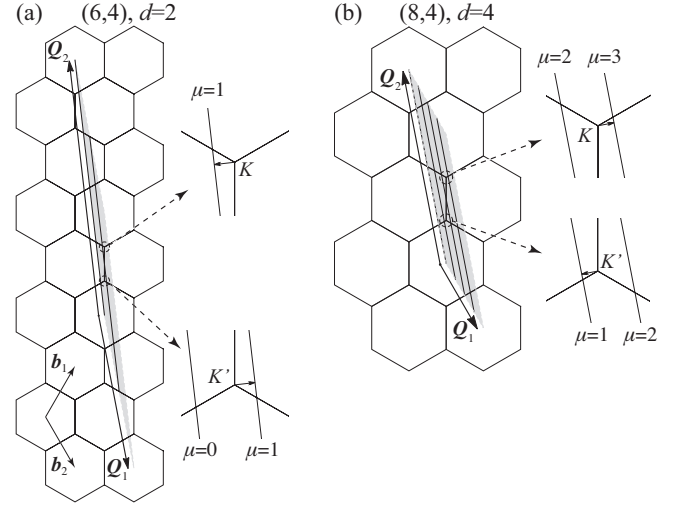


FIG. 1. Cutting lines for (a) $(n, m) = (6, 4)$ ($d = 2$, type-1) and (b) $(n, m) = (8, 4)$ ($d = 4$, type-2) s-SWNT. The integers are chosen as (a) $(p, q) = (2, 1)$ and (b) $(p, q) = (1, 0)$. Shadow areas show 2D BZ given by two reciprocal lattice vectors \mathbf{Q}_1 and \mathbf{Q}_2 . Dashed circles show K and K' points closest to the cutting lines. Right insets in each figure show enlarge near K and K' points. Arrows from K and K' points show $\pm \mathbf{K}_1/3$ to the nearest cutting lines.

point the orbital angular momentum of K (K') valley for the s-SWNTs. From Eq. (12), the closest cutting line to the K point is given by

$$\mu_1 = \text{mod} \left(\frac{2n+m \mp 1}{3}, d \right), \quad (13)$$

and that to the K' point is given by

$$\mu_{1'} = \text{mod} \left(-\frac{2n+m \mp 1}{3}, d \right). \quad (14)$$

Therefore, the condition that the two cutting lines μ_1 and $\mu_{1'}$ are identical is expressed by,

$$\text{mod} \left(2 \times \frac{2n+m \mp 1}{3}, d \right) = 0. \quad (15)$$

Since both n and m are multiple of d , Eq. (15) holds only for $d = 1$ and $d = 2$. For the s-SWNTs with $d \geq 4$, μ_1 and $\mu_{1'}$ are nonequivalent. (See cutting lines in Fig. 1, as examples for $d = 2$ and $d = 4$.) Here we exclude the case of $d = 3$, which holds only for a part of m-SWNTs. For $d = 1$, $\mu_1 = \mu_{1'} = 0$. For $d = 2$, we get $\mu_1 = \mu_{1'} = 1$ because they cannot be 0 by their definitions for $d \geq 2$. It is also known from Eq. (12) that a point k_1 ($k_{1'}$) on the line μ_1 ($\mu_{1'}$), at which the bottom of the conduction band and the top of the valence band appears from K (K') valley, is given by

$$k_1 = \frac{2\pi}{3a_z} \text{mod} \left(2p+q \mp \frac{\Delta\theta}{2\pi}, 3 \right), \quad (16)$$

$$k_{1'} = \frac{2\pi}{3a_z} \text{mod} \left[- \left(2p+q \mp \frac{\Delta\theta}{2\pi} \right), 3 \right]. \quad (17)$$

The cutting lines and the 1D k points closest to K and K' points are summarized in Table I.

TABLE I. Cutting lines μ and 1D k points closest to K and K' points. The values of μ and k are given in $\mu = 1, \dots, d-1$ and $0 \leq k < 2\pi/a_z$, respectively. Here $d = \gcd(n, m)$, $d_R = \gcd(2n+m, 2m+n)$, p and q are given by Eq. (1), a_z and $\Delta\theta$ are given in Eqs. (2) and (3), respectively. The sign $-$ and $+$ in μ_1 , $\mu_{1'}$, k_1 and $k_{1'}$ applied for type-1 [$\text{mod}(2n+m, 3) = 1$] and type-2 [$\text{mod}(2n+m, 3) = 2$] s-SWNTs, respectively.

Type	Cutting line and 1D k point closest to K and K'
Semiconducting SWNTs [$\text{mod}(2m+n, 3) = 1, 2$]	
	$\mu_1 = \text{mod}\left(\frac{2n+m+1}{3}, d\right)$, $\mu_{1'} = \text{mod}\left(-\frac{2n+m+1}{3}, d\right)$
	$k_1 = \frac{2\pi}{3a_z} \text{mod}\left(2p+q \mp \frac{\Delta\theta}{2\pi}, 3\right)$
	$k_{1'} = \frac{2\pi}{3a_z} \text{mod}\left[-(2p+q \mp \frac{\Delta\theta}{2\pi}), 3\right]$
$d = 1$	$\mu_1 = \mu_{1'} = 0$
$d = 2$	$\mu_1 = \mu_{1'} = 1$
$d \geq 4$	$\mu_1 \neq \mu_{1'}$
Metallic SWNTs [$\text{mod}(2m+n, 3) = 0$]	
	$\mu_K = \text{mod}\left(\frac{2n+m}{3}, d\right)$, $\mu_{K'} = \text{mod}\left(-\frac{2n+m}{3}, d\right)$
	$k_K = \frac{2\pi}{3a_z} \text{mod}(2p+q, 3)$, $k_{K'} = \frac{2\pi}{3a_z} \text{mod}(-2p-q, 3)$
metal-1 ($d_R = d$)	$\mu_K \neq \mu_{K'}$
metal-2 ($d_R = 3d$)	$\mu_K = \mu_{K'} = 0$
	$k_K = \frac{4\pi}{3a_z}$, $k_{K'} = \frac{2\pi}{3a_z}$ [if $\text{mod}\left(\frac{m}{d}, 3\right) = 1$]
	$k_K = \frac{2\pi}{3a_z}$, $k_{K'} = \frac{4\pi}{3a_z}$ [if $\text{mod}\left(\frac{m}{d}, 3\right) = 2$]

Figure 2 shows the classification of SWNTs up to $2n+m = 78$. The ratio of the metal-2 nanotubes in the m-SWNTs, for both left and right handedness,³² in $0.5\text{nm} < d_t < 3\text{nm}$ is about 75%, and that of $d \leq 2$ nanotubes in the s-SWNTs is about 85%. This indicates that the two valleys have the same angular momentum in the majority (82%) of SWNTs. (See Fig. 2 (b) for the ratios.)

It is expected that finite-length s-SWNTs with $d \geq 4$, as well as the metal-1 nanotubes with $d \geq 3$,²² with C_d rotational symmetry exhibit fourfold degeneracy since μ and $d - \mu$, which is equivalent to $-\mu$, states degenerate under the time reversal symmetry, and the cutting lines closest to K and K' are inequivalent for $d \geq 3$. It is important to note that the fourfold degeneracy is lifted by the spin-orbit interaction that keeps the time-reversal symmetry,²⁰ which will be confirmed in numerical calculation presented in the Appendix A. On the other hand, for finite-length s-SWNTs with $d \leq 2$, as well as the metal-2 nanotubes,²² the strong valley coupling can occur, which breaks the valley degeneracy regardless of spin-orbit interaction, even the boundary is clean so as to keep the rotational symmetry of bulk, which will be shown in the next section.

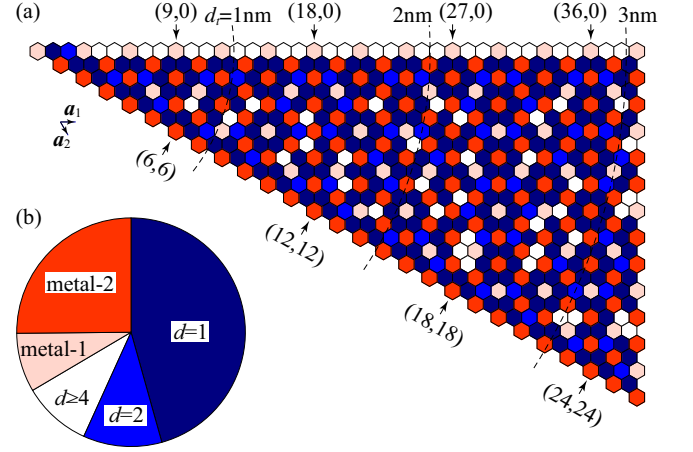


FIG. 2. (Color online) Classification of single-wall carbon nanotubes by means of angular momenta of two valleys. (a) A hexagon pointed by the chiral vector $n\mathbf{a}_1 + m\mathbf{a}_2$ from the leftmost hexagon represents (n, m) nanotube. Hexagons with pink (red) denotes metal-1 (metal-2) nanotubes. Hexagons with navy (blue) denotes $d = 1$ ($d = 2$) s-SWNTs, and white hexagons denotes $d \geq 4$ s-SWNTs. Hexagons with dark colors (navy, blue and red) denote SWNTs, in which two valleys have the same angular momentum $\mu = 0$ (navy and red) or $\mu = 1$ (blue). Hexagons with light colors (pink and white) denote SWNTs, in which two valleys have different angular momenta. The dashed curves show the borders indicating the corresponding diameters of nanotubes, $d_t = 1, 2$, and 3 nm. (b) Pie chart of ratios of $d = 1$, $d = 2$, $d \geq 4$ of s-SWNTs, and metal-1 and metal-2 nanotubes for both left and right handedness in $0.5\text{nm} < d_t < 3\text{nm}$.

III. VALLEY COUPLING IN FINITE-LENGTH S-SWNTS

In this section, we will show features of valley coupling in the numerical calculation of the energy levels of finite-length s-SWNTs with $d \leq 2$.

In Fig. 3 (a), we show the numerically calculated energy levels ε_l near the highest occupied molecular orbital (HOMO), where l is the index of the energy level numbered from HOMO ($l = 0$) in ascending order of the energy for (7,3) nanotube of 50.18 nm length. Here the origin of the energy is set to be $(\varepsilon_{l=1} + \varepsilon_{l=0})/2 = 0$. The boundary is constructed by terminating at the plane orthogonal to the nanotube axis and removing Klein-type terminations at which terminated site neighbors two empty sites. This is categorized as the minimal boundary, in which the edge structure is selected to have minimum numbers of empty sites [dashed circles in Fig. 5 (a)] and dangling bonds, and these numbers are the same,³⁶ for both ends. The diagrammatic picture of the left end is shown in Fig. 5 (a). The calculation is done using the extended tight-binding method for the finite-length nanotubes,²² in which π and σ orbitals of carbon atom are taken into account, and the hopping and the overlap integrals between two atoms evaluated by the *ab initio* calculation³⁷ for interatomic distance up to 10 bohr ($\sim 5\text{\AA}$) in

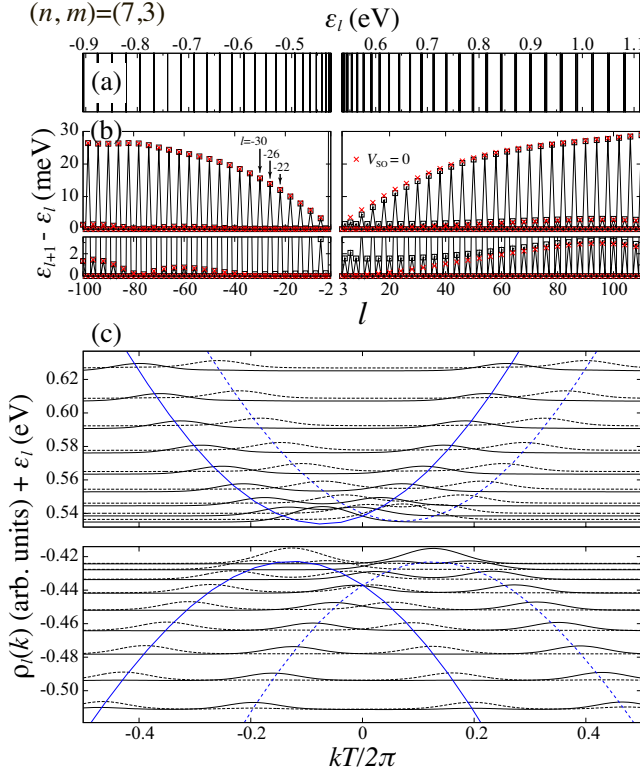


FIG. 3. (Color online) Energy levels and eigenstates for (7,3) nanotube ($d = 1$, type-2) of 50.18 nm length. (a) Energy levels ε_l from valence ($\varepsilon_l \leq -0.424$ eV, $l \leq -2$) and conduction ($\varepsilon_l \geq 0.535$ eV, $l \geq 3$) bands, where l is the level index. (b) Level separation $\varepsilon_{l+1} - \varepsilon_l$ as a function of level index l . The case of absence of spin-orbit interaction is shown by the red cross. To show the nearly fourfold degeneracy clearly, $l = -30, -26, -22$ are indicated by arrows. (c) Intensity plot of Fourier transforms of wave functions at A sublattice for spin-up majority states. The energy for each level ε_l is added for each intensity plot. They are presented by either solid or dashed lines in turn as increasing the energy to show them clearly. The blue solid and the blue dashed lines show the energy band calculation under the periodic boundary condition near the K and the K' valleys, respectively.

the three-dimensional structure are included. The optimized position of carbon atoms is utilized from the previous calculation.²⁰ To eliminate the dangling bonds in the numerical calculation, each single dangling bond at the ends is terminated by a hydrogen atom. The atomic spin-orbit interaction on each carbon atom are taken into account.²⁰ Unless otherwise indicated, the value of $V_{SO} = 6$ meV for the atomic spin-orbit interaction is used in the calculation.

The energy levels of $\varepsilon_l \leq -0.424$ eV ($l \leq -2$), which are originated from the valence band, and $\varepsilon_l \geq 0.535$ eV ($l \geq 3$), originated from the conduction band, are shown in Fig. 3 (a). In the energy gap, there are fourfold degenerate localized states near the ends ($l = -1, 0, 1, 2$), two spin degenerate states polarized at B sublattices at left end and two spin degenerate states polarized at A sub-

lattices at right end, at $\varepsilon = 0$, not shown in the figure), known as the edge states,^{38–41} which will be discussed in Sec. IV C. Due to the hopping to next nearest neighbor and farther sites, the localized states appear below the center of the energy gap.⁴² As increasing (decreasing) the energy from the bottom of the conduction band (the top of the valence band), the level separation, $\varepsilon_{l+1} - \varepsilon_l$, gradually increases to the constant value reflecting the changing from the quadratic to linear energy dispersion of the energy bands, as shown in Fig. 3 (b). The energy levels are nearly degenerate in fourfold. In Fig. 3 (c), we show intensity plot of Fourier transform of wavefunction on A sublattice for each level as a function of k . [A tiny magnetic field ($B = 10^{-6}$ T, corresponding spin splitting is $\sim 10^{-8}$ meV) parallel to the nanotube axis is applied to extract the spin-up majority states in the numerical calculation. The intensity plot is zone-folded in the 1D BZ of nanotube and is smoothed by a Gaussian function.] The fourfold degeneracy reflects the decoupling of the two valleys, which is confirmed that each eigenstate is formed from leftgoing and rightgoing states in a single valley, as shown in Fig. 3 (c). The small lift of the fourfold degeneracy, shown in lower panel of Fig. 3 (b), is due to the spin-orbit interaction and the small valley coupling in the finite-length effect, as seen in the finite-length metal-2 nanotubes.²²

For comparison in Fig. 3, the energy levels ε_l and level separation $\varepsilon_{l+1} - \varepsilon_l$ for (6,4) nanotube of 50.14 nm length with a minimal boundary are shown in Figs. 4 (a) and 4 (b), respectively. As in the case of Fig. 3, the energy levels for the four edge states exist within the energy gap at $\varepsilon_l = 0$ for $l = -1, 0, 1, 2$, two states polarized at B sublattices at left end and two states polarized at A sublattices at right end (not shown in the figure). In contrast to the case of Fig. 3, except near the bottom or the top of the energy gap, the energy levels show twofold degeneracy reflecting the strongly couple of two valleys, which is confirmed in the intensity plot of Fig. 4 (c). The oscillatory behavior of two- and fourfold degeneracies reflects the asymmetric group velocity in the same valley, as seen in the m-SWNTs.^{22,43} The behaviors of decoupling or strong coupling of two valleys demonstrated by the numerical calculation can be understood by the effective 1D lattice model, which is discussed in the next section.

IV. EFFECTIVE 1D LATTICE MODEL

An effective 1D lattice model, which includes only the nearest neighbor hopping term for the spinless case, exhibits not only the microscopic mechanism of valley coupling but also the number of edge states appearing in the energy gap.

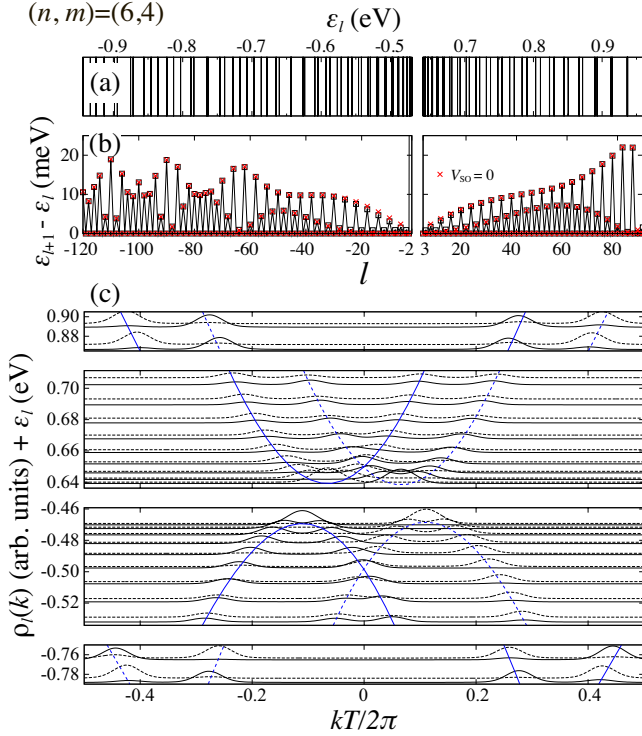


FIG. 4. (Color online) Energy levels and eigenstates for (6,4) nanotube ($d = 2$) of 50.14 nm length. (a) Energy levels ε_l from valence ($\varepsilon_l \leq -0.469$ eV, $l \leq -2$) and conduction ($\varepsilon_l \geq 0.639$ eV, $l \geq 3$) bands, where l is the level index. (b) Level separation $\varepsilon_{l+1} - \varepsilon_l$ as a function of level index l . (c) Intensity plot of Fourier transforms of wave functions of A sublattice for spin-up majority states. The blue solid and dashed lines show the energy band calculation under the periodic boundary condition near the K and K' valleys, respectively.

A. Derivation of effective 1D lattice model

First, we derive an effective 1D lattice model for each angular momentum (e.g., $\mu = 0$ for $d = 1$, $\mu = 0$ and $\mu = 1$ for $d = 2$ s-SWNTs) from the nearest neighbor tight-binding Hamiltonian. To derive the effective model, we restrict ourselves in the nearest neighbor tight-binding model for π electrons, $H = \sum_{\mathbf{r}} \sum_{j=1}^3 \gamma_j c_{\mathbf{A},\mathbf{r}}^\dagger c_{\mathbf{B},\mathbf{r}+\mathbf{\Delta}_j} + \text{H.c.}$, where $c_{\sigma,\mathbf{r}}^\dagger$ ($c_{\sigma,\mathbf{r}}$) is the creation (annihilation) operator of π electron on σ atom ($\sigma = \text{A, B}$) at site \mathbf{r} , $\mathbf{\Delta}_j$ is the vector from A to nearest j -th B atom ($j = 1, 2, 3$), and γ_j is the hopping integral between A and j -th B atom. The atom position is expressed by the two unit vectors as $\mathbf{r} = \nu \mathbf{C}_h/d + \ell \mathbf{R}$, where $\nu = 0, 1, \dots, d-1$, and the integer ℓ points the lattice position in the axis direction in units of a_z .

By employing the Fourier transform in the \mathbf{Q}_1 direction to the operator,

$$c_{\sigma(\mu,\ell)} = \frac{1}{\sqrt{d}} \sum_{\nu=0}^{d-1} \exp\left(-i\frac{\mu}{d}\mathbf{Q}_1 \cdot \nu \frac{\mathbf{C}_h}{d}\right) c_{\sigma,\mathbf{r}}, \quad (18)$$

the Hamiltonian is decomposed into projected Hamiltonian for μ -th angular momentum, $H = \sum_{\mu=0}^{d-1} H_{\mu}$, $H_{\mu} = \sum_{\ell} \sum_{j=1}^3 \gamma_j e^{i\frac{2\pi}{d}\Delta\nu_j\mu} c_{\mathbf{A}(\mu,\ell)}^\dagger c_{\mathbf{B}(\mu,\ell+\Delta\ell_j)} + \text{H.c.}$ Here $\Delta\nu_j$ and $\Delta\ell_j$ for the three nearest neighbor carbon atoms are the \mathbf{C}_h/d and \mathbf{R} components of $\mathbf{\Delta}_j$, respectively, and their explicit forms are $\Delta\nu_1 = (p-q)/3$, $\Delta\nu_2 = -(2p+q)/3$, $\Delta\nu_3 = 2q+p/3$, and $\Delta\ell_j = -(n-m)/3d$, $(2n+m)/3d$, $-(2m+n)/3d$ for $j = 1, 2, 3$, respectively. By extracting the relevant H_{μ} , one gets an effective 1D Hamiltonian.

For the s-SWNTs, as well as the metal-1 nanotubes, since $\Delta\ell_j$ and $\Delta\nu_j$ are fractional numbers with three as the denominator, translation conversion of the coordinate for B sublattice such as $\mathbf{\Delta}_1 \rightarrow 0$ would be convenient. This conversion makes A and B sublattices terminated at the same $\ell = 1$ site, which is convenient for topological discussion which will be given in Sec. IV C. Further, this conversion makes the hopping integrals in the Hamiltonian real numbers for $d = 1$ and $d = 2$ cases, as shown below. The Hamiltonian is modified under this conversion, $H_{\mu} \rightarrow H_\mu$, where

$$H_\mu = \sum_{\ell} \sum_{j=1}^3 \gamma_j e^{i\frac{2\pi}{d}\Delta\nu'_j\mu} c_{\mathbf{A}(\mu,\ell)}^\dagger c_{\mathbf{B}(\mu,\ell+\Delta\ell'_j)} + \text{H.c.} \quad (19)$$

where

$$\Delta\ell'_1 = 0, \quad \Delta\ell'_2 = \frac{n}{d}, \quad \Delta\ell'_3 = -\frac{m}{d}, \quad (20)$$

and

$$\Delta\nu'_1 = 0, \quad \Delta\nu'_2 = -p, \quad \Delta\nu'_3 = q. \quad (21)$$

The connection diagram of the effective 1D lattice model H_μ is depicted in Figs. 5 (a) and 5 (b) for $(n/d, m/d) = (7, 3)$ and $(3, 2)$, respectively. The solid lines show the hopping between atoms. The solid circles represent the carbon atoms at the boundary, the dashed circles represent the empty atomic sites and the dashed lines represent the missing bonds.

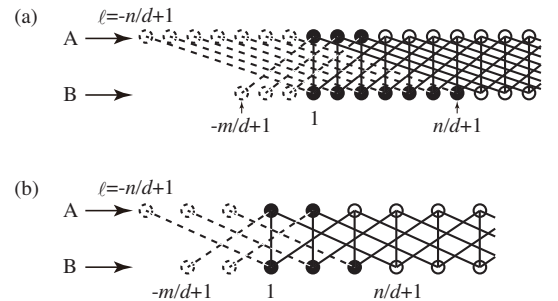


FIG. 5. Bond connection diagram of effective 1D lattice model H_μ and left end with minimal boundary for (a) $(n/d, m/d) = (7, 3)$, and (b) $(n/d, m/d) = (3, 2)$.

B. Eigenstate

To understand the coupling of two valleys in the eigenstates, we will show how the eigenstates are constructed from the leftgoing and rightgoing traveling waves in the two valleys using the effective 1D model. Hereafter, 1D lattice site of the effective 1D model is measured in units of a_z , for simplicity, and 1D wavenumber is therefore measured in units of $1/a_z$.

For an eigenstate with energy ε of H_μ , which has the amplitude $\phi_{\sigma\ell}$ at σ -atom on ℓ -site satisfying the solution of $\phi_{\sigma\ell+t} = \lambda^t \phi_{\sigma\ell}$, $\phi_{B\ell} = \eta \phi_{A\ell}$,²² we have the following simultaneous equations for λ and η ,

$$1 + e^{i\frac{2\pi}{d}p\mu} \lambda^{-\frac{n}{d}} + e^{-i\frac{2\pi}{d}q\mu} \lambda^{\frac{m}{d}} = \frac{\varepsilon}{\gamma} \eta, \quad (22)$$

$$1 + e^{-i\frac{2\pi}{d}p\mu} \lambda^{\frac{n}{d}} + e^{i\frac{2\pi}{d}q\mu} \lambda^{-\frac{m}{d}} = \frac{\varepsilon}{\gamma} \frac{1}{\eta}. \quad (23)$$

Assumption of using the same hopping integrals $\gamma = \gamma_j$ is safely acceptable for the s-SWNTs, unlike the m-SWNTs²² in which narrow gap is induced by the small difference among γ_j reflecting the curvature of nanotube surface. The simultaneous equations have $2(n/d + m/d)$ sets of solutions (λ, η) because each equation is the $(n/d + m/d)$ th degree equation. We call A (B) mode for a mode with $|\eta| < 1$ ($|\eta| > 1$) because the wavefunction is polarized at the A (B) sublattice. A mode with $|\lambda| < 1$ ($|\lambda| > 1$) is a evanescent mode at the left (right) side, and a mode with $|\lambda| = |\eta| = 1$ is a traveling mode which extends in whole of the system.

In the low energy limit $|\varepsilon/\gamma| \ll 1$, the roots of left hand side of Eq. (22) [Eq. (23)] gives λ for the A [B] modes. As shown in the Appendix B1, the number of evanescent modes at the left end for σ sublattice, N_σ , are given by counting the number of roots in between two outermost roots, which correspond to the modes with the longest decay length, in the unit circle centered at the origin in the complex plane, as follows;

$$N_A = \left\lfloor \frac{2n+m}{3d} \right\rfloor + n_A, \quad N_B = \left\lfloor \frac{n+2m}{3d} \right\rfloor + n_B, \quad (24)$$

where $\lfloor x \rfloor$ is the floor function giving the greatest integer that is less than or equal to x , and $(n_A, n_B) = (0, 1)$ [(1, 0)] for the cases of $\text{mod}(2n/d + m/d, 3) = 1$ and $|\mu/d - 1/2| > 1/6$ [$< 1/6$], or, $\text{mod}(2n/d + m/d, 3) = 2$ and $|\mu/d - 1/2| < 1/6$ [$> 1/6$]. The integers n_σ are summarized in Table II.

When the energy increases (decreases) from $\varepsilon = 0$, the evanescent modes with the longest decay length change to the traveling modes, as shown in Fig. 6. Let us explicitly consider the cases of $d = 1$ where $\mu = 0$ is only the independent cutting line, and $\mu = 1$ for $d = 2$, for which H_μ contains the states closest to both K and K' points, as discussed in Sec. II. Since the modes we focus on are closest to

$$\lambda_\tau = \exp(i\tau k_1), \quad (25)$$

TABLE II. Integers n_σ in Eq. (24) for given type of s-SWNTs, $\text{mod}(2n/d + m/d, 3)$ and for given angular momentum μ , at $\varepsilon = 0$.

	$\text{mod}(2\frac{n}{d} + \frac{m}{d}, 3) = 1$		$\text{mod}(2\frac{n}{d} + \frac{m}{d}, 3) = 2$	
	$0 \leq \frac{\mu}{d} < \frac{1}{3}$	$\frac{1}{3} < \frac{\mu}{d} < \frac{2}{3}$	$0 \leq \frac{\mu}{d} < \frac{1}{3}$	$\frac{1}{3} < \frac{\mu}{d} < \frac{2}{3}$
	or $\frac{2}{3} < \frac{\mu}{d} < 1$		or $\frac{2}{3} < \frac{\mu}{d} < 1$	
n_A	0	1	1	0
n_B	1	0	0	1

where $\tau = 1$ (-1) denotes the K (K') valley and k_1 is the wavenumber for the state closest to the K point given in Eq. (16), by employing the similar analysis for the m-SWNTs with narrow gap given in Appendix D of Ref. 22, these modes are given by expanding Eqs. (22) and (23) near λ_τ . (The detailed calculation for the modes is given in Appendix B2.)

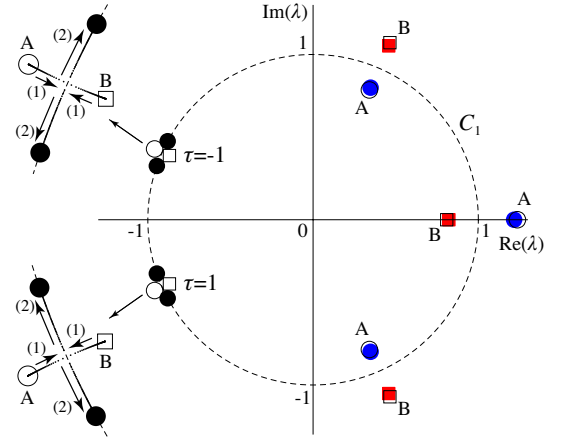


FIG. 6. (Color online) Solutions λ for Eqs. (22) and (23) in the complex plane for $(n, m) = (6, 4)$, ($d = 2$, type-1), $\mu = 1$, $p = 2$, $q = 1$. Modes near $\lambda = \lambda_\tau = e^{i\tau k_1}$ are labeled by $\tau = \pm 1$, where $k_1 = 1.13\pi$. Dashed circle C_1 shows the unit circle centered at the origin. Blue and red filled marks are the solutions for A and B modes, respectively, and black filled circles on C_1 are the solutions for the traveling modes, at $|\varepsilon/\gamma| = 0.4$. Open circles (squares) show the solutions for A (B) modes at $\varepsilon = 0$. Insets show the enlargements near $\lambda_\tau = \pm 1$, and the dots between the open and filled marks show the solutions for the energies in $0 \leq |\varepsilon/\gamma| \leq 0.4$ with energy interval of $0.4|\gamma|/100$. Transition from evanescent modes to traveling modes occurs at $|\varepsilon/\gamma| = \varepsilon_{\text{gap}}/2 = 0.21$. Arrows and numbers show the changing of the modes when $|\varepsilon|$ increases in (1) $0 \leq |\varepsilon| \leq \varepsilon_{\text{gap}}/2$, and (2) $|\varepsilon| \geq \varepsilon_{\text{gap}}/2$.

At $\varepsilon = 0$, the B (A) modes with

$$\lambda_{\tau,0} = \exp\left(i\tau k_1 - \frac{2a_z}{3d_t}\right) \quad (26)$$

are the modes with the longest decay length for the type-1 (type-2) s-SWNTs. When the energy increases (decreases) to $\varepsilon = b\varepsilon_{\text{gap}}/2$, which corresponds to the energy bottom (top) of the conduction (valence) band for $b = 1$

($b = -1$), the mode of the longest decay length together with the conjugated mode $[(\lambda, \eta) \leftrightarrow (1/\lambda^*, 1/\eta^*)]$ are continuously changing to the doubly degenerate modes with $\lambda = \lambda_\tau$ at each τ valley, where $\varepsilon_{\text{gap}} = 2|\gamma|a/\sqrt{3}d_t$. When the energy increases or decreases further to

$$\varepsilon = b|\gamma|\frac{\sqrt{3}a}{2a_z}\sqrt{k^2 + \left(\frac{2a_z}{3d_t}\right)^2}, \quad (27)$$

the doubly degenerate modes split into the leftgoing ($r = -1$) and rightgoing ($r = 1$) traveling modes with

$$\lambda_{\tau rk} = \exp[i(\tau k_1 + rk)] \quad (28)$$

at each τ valley, where $k > 0$. The above changing of the modes is seen in Fig. 6 in the λ complex plane for $(n, m) = (6, 4)$, $d = 2$ and $\mu = 1$ [see the modes labeled by $\tau = 1$ ($\tau = -1$), which correspond to the modes of K (K') valley]. During the energy changing, the other modes remain almost unchanged, as shown that the filled and open marks are overlapped in Fig. 6. Since the two evanescent modes of B [A] sublattice at the zero energy change to the traveling modes above and below the energy gap, the integers N_σ is now given by Eq. (24) with $(n_A, n_B) = (0, -1)$ $[(-1, 0)]$ for the type-1 [type-2] s-SWNTs. The integers n_σ for the energy inside and outside the energy gap are summarized in Table III.

TABLE III. Integers n_σ in Eq. (24) for the energy inside and outside the energy gap, for $d = 1$ ($\mu = 0$) and $\mu = 1$ of $d = 2$ cases.

	Type-1 s-SWNTs		Type-2 s-SWNTs	
	$ \varepsilon < \frac{\varepsilon_{\text{gap}}}{2}$	$ \varepsilon > \frac{\varepsilon_{\text{gap}}}{2}$	$ \varepsilon < \frac{\varepsilon_{\text{gap}}}{2}$	$ \varepsilon > \frac{\varepsilon_{\text{gap}}}{2}$
n_A	0	0	1	-1
n_B	1	-1	0	0

The wavefunction near the left end is written as the linear combination of the relevant modes ($|\lambda| \leq 1$). Above and below the energy gap, the wavefunction is written as

$$\phi_{\sigma k}^b(\ell) = \sum_{\tau} g_{\sigma \tau k}^b(\ell) e^{i\tau k_1 \ell} + \sum_{m_\sigma=1}^{N_\sigma} c_{\sigma m_\sigma} (\lambda_{\sigma m_\sigma}^<)^\ell, \quad (29)$$

where $\lambda_{\sigma m_\sigma}^<$ denotes the evanescent modes of σ sublattice at the left end which satisfy $|\lambda_{\sigma m_\sigma}^<| < 1$, and

$$g_{\sigma \tau k}^b(\ell) = \sum_r c_{\sigma \tau rk}^b e^{ir k \ell} \quad (30)$$

is the envelope function for the fast oscillating mode, $e^{i\tau k_1 \ell}$. Here we have the relation

$$c_{B \tau rk}^b = e^{i\Phi_{\tau rk}^b} c_{A \tau rk}^b, \quad (31)$$

where $\Phi_{\tau rk}^b$ is the phase difference between A and B sublattices for the traveling mode. [The explicit expression of $\Phi_{\tau rk}^b$ is given in Eq. (B23) in Appendix B 2.]

Under the boundary conditions, constriction on the coefficients of the traveling modes is determined. As shown in Figs. 5 (a) and (b), the following conditions hold for the minimal boundary,

$$\phi_{Ak}^b(\ell) = 0 \text{ at } \ell = -n/d + 1, \dots, 0, \quad (32)$$

$$\phi_{Bk}^b(\ell) = 0 \text{ at } \ell = -m/d + 1, \dots, 0. \quad (33)$$

For the case of $n > m \geq 0$, except for $m = n - 2$, the number of the boundary conditions for A sublattice, n/d , is larger or equal to that of the relevant modes, the two fast oscillating modes and N_A evanescent modes, $N_A + 2$. For $(n, m) = (7, 3)$ as an example, the number of relevant modes for A sublattice is $N_A + 2 = 6$ and that of boundary conditions for A sublattice is $n/d = 7$ in $|\varepsilon| > \varepsilon_{\text{gap}}/2$. For this case, the boundary conditions Eq. (32) act as the “fixed boundary condition” for the envelope function of A sublattice, which force the envelope function zero near the left end, $g_{A \tau k}^b(\ell \rightarrow 0) = 0$. To satisfy this condition, the wavefunctions are formed from the leftgoing and rightgoing traveling modes within the same valley with the same amplitude, in order to have the following functional form,

$$g_{A \tau k}^b(\ell) \propto \sin(k\ell). \quad (34)$$

Since the boundary conditions are satisfied by constructing the eigenfunctions in each valley separately, two valleys are decoupled and the valley degeneracy occurs. When the spin-orbit interaction turns on, Eq. (34) is satisfied for one of the two valleys while the component of another valley is vanished, as seen in Fig. 3 (c).

For the case of $m = n - 2$, the number of boundary conditions is one less than that of the relevant modes for both A and B sublattice, $n/d = N_A + 1$ and $m/d = N_B + 1$. For the case of $\mu = 1$ of $(n, m) = (6, 4)$, as an example, the numbers of boundary conditions for the A and B sublattices are $n/d = 3$ and $m/d = 2$, respectively, and that of relevant modes in A and B sublattices are $N_A + 2 = 4$ and $N_B + 2 = 3$, respectively, in $|\varepsilon| > \varepsilon_{\text{gap}}/2$. Therefore, the wavefunctions for A and B sublattices can be determined with an arbitrariness of the amplitude. In addition, by employing the similar analysis of our previous study for the m-SWNTs,²² which is given in Appendix B 3, it is shown that the coefficients satisfy $|c_{\sigma, \tau=1, r, k}^b| = |c_{\sigma, \tau=-1, -r, k}^b|$ and $c_{\sigma, \tau=1, -r, k}^b = c_{\sigma, \tau=-1, r, k}^b = 0$, or equivalently, the first term in Eq. (29) is written as

$$\phi_{\sigma k}^b(\ell) \propto e^{i(k_1 + rk)\ell} + e^{-i(k_1 + rk)\ell} e^{-i\varphi} \quad (35)$$

for either $r = 1$ or $r = -1$ in the linear dispersion region in which the relation $|\Phi_{\tau rk}^b - \Phi_{\tau -rk}^b| = \pi$ holds, where φ is the phase difference between the two traveling modes, $\varphi = \arg c_{\sigma, \tau=1, r, k}^b - \arg c_{\sigma, \tau=-1, -r, k}^b$. Therefore, we have the strong coupling of two valleys, as in the case of the armchair nanotubes or the chiral metal-2 SWNTs with so-called the orthogonal boundary.²² Near the top of the valence band and bottom of the conduction band, on the

other hand, two valleys are decoupled since the eigenstates are constructed from the leftgoing and rightgoing states in the same valley to satisfy the boundary conditions, as also discussed in details in Appendix B 3. It should be noted that the strong valley coupling could occur for the other chiralities than $m = n - 2$ for the s-SWNTs with other boundaries, as in the case of the metal-2 nanotubes.²²

For the case of $m > n \geq 0$, the case of zigzag-left handedness, the similar discussion with above is employed: we have the fixed boundary condition for the envelop function of B sublattice at the left end, except for the case of $m = n + 2$ in which the strong valley coupling occurs.

C. Edge state

The number of edge states appeared at $\varepsilon = 0$ is evaluated by the difference between the number of independent evanescent modes and the number of boundary conditions, as in the case of previous discussions for graphene with certain boundaries³⁶ and for the m-SWNTs.²² For the case of $n > m \geq 0$, the number of edge states which are localized at A and B sublattices at the left end are given by,

$$N_{\text{edge}}^{(\text{L,A})} = 0, \quad N_{\text{edge}}^{(\text{L,B})} = N_B - \frac{m}{d}, \quad (36)$$

respectively, for each μ and each spin state. Since the number of boundary conditions is larger or equal to that of the relevant modes for A sublattice, the number of edge states for A sublattice is zero. As shown in Appendix B 4, these edge states appear only at $\varepsilon = 0$. The numbers of edge states are estimated using Eq. (24) with Table II. For instance, $N_{\text{edge}}^{(\text{L,B})} = 1$ in $(n, m) = (7, 3)$ nanotube. For $(6, 4)$ nanotube, $N_{\text{edge}}^{(\text{L,B})} = 0$ for $\mu = 0$ and $N_{\text{edge}}^{(\text{L,B})} = 1$ for $\mu = 1$. Since the numbers estimated by Eq. (36) give the edge states for each spin and each end, therefore total number of edge states is 4 for both $(7, 3)$ and $(6, 4)$ nanotubes, which is consistent with the numerical calculation in Figs. 3 and 4.

As an alternative way to evaluate the number of edge states, we can employ the theory of topological categorization for the bulk systems.^{44,45} The winding number is frequently discussed in topological insulating materials. For the SWNTs, the winding number for the angular momentum μ , w_μ , is given by

$$w_\mu = \frac{1}{2\pi} \int_0^{2\pi} dk \frac{\partial \arg f_\mu(k)}{\partial k}, \quad (37)$$

where $f_\mu(k)$ is the off-diagonal term of the Hamiltonian matrix of H_μ ,

$$f_\mu(k) = \langle Ak\mu | H_\mu | Bk\mu \rangle = \sum_{j=1}^3 \gamma_j e^{i\frac{2\pi}{d} \Delta \nu'_j \mu} e^{ik \Delta \ell'_j}, \quad (38)$$

$|\sigma k\mu\rangle$ is the Bloch state of σ sublattice with wavenumber k and the angular momentum μ . Since the integral of Eq. (38) gives phase accumulation from $k = 0$ to $k = 2\pi$ for the function with 2π periodicity, the winding number of Eq. (37) is an integer. Further, under continuous changing of the system parameters such as the hopping integrals γ_j , the winding number is invariant, staying at an integer value, as long as it is well-defined value. In fact, the winding number is well-defined value for a system with a finite energy gap, in which $f_\mu(k)$ is finite value for any k and then $\arg f_\mu(k)$ is well-defined value for any $0 \leq k < 2\pi$. Note that energy gap closes at k , at which $f_\mu(k) = 0$ and thus $\arg f_\mu(k)$ cannot be defined. When a metallic phase appears during the changing of system parameters, we may have a topological phase transition, which could be induced by applying the magnetic field for m-SWNTs with narrow energy gap.^{22,46}

The winding number has been widely used as the number of edge states for the topological systems, as well as other topological invariants, in the context of categorization of materials by their topological properties.⁴⁷⁻⁴⁹ For the integer quantum Hall systems, it is well-known that the filling number of the Landau levels as the bulk quantity, which is known to be a topological invariant called Chern number,^{50,51} and the number of edge channels have one-to-one correspondence.⁵²⁻⁵⁵ For 1D systems, on the other hand, only a few examples^{45,56-58} are known to show exact one-to-one correspondence of the winding number and the number of edge states, so-called bulk-edge correspondence, which would be important for better understanding of the topological materials. Here we will show the bulk-edge correspondence: the winding number is the number of edge states for the s-SWNTs by using the results from the analysis in Sec. IV B with a theorem in the complex analysis.

First, we show the numerically evaluated w_μ values for s-SWNTs of $(n, m) = (7, 3)$ and $(6, 4)$. Figure 7 shows the phases of $f_\mu(k)$ in for (a) $(n, m) = (7, 3)$ and (b) $(6, 4)$, which is plotted on torus in which circumferential direction correspond to argument of $f_\mu(k)$ as a function of k in the direction around the torus, to show the “winding” property clearly, in $0 \leq k < 2\pi$ and $0 \leq \arg f_\mu < 2\pi$. For both cases, the total winding number, how many times the curves winds around the circumference direction, is one. Therefore, the total edge states including both ends and two spin states is estimated to be four, which is consistent with the numerical calculation showing the edge states at $l = -1, 0, 1, 2$.

Let us show that the number of edge states estimated from the mode analysis shown in Eq. (36) and the winding number in Eq. (37) is identical for the s-SWNTs. This “bulk-edge correspondence” is proven by using the following theorem known as Cauchy’s argument principle in the complex analysis,

$$\oint_C d\lambda \frac{\partial \log F(\lambda)}{\partial \lambda} = 2\pi i(n_r - n_p), \quad (39)$$

where n_r and n_p are the number of complex roots and

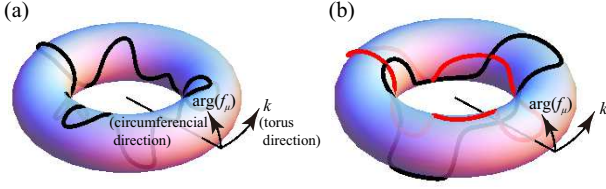


FIG. 7. (Color online) Phase of matrix element f_μ on torus of k - $\arg(f_\mu)$ face for (a) $(n, m) = (7, 3)$ and for (b) $(6, 4)$, $\mu = 0$ (black) and $\mu = 1$, $p = 2$, $q = 1$ (red).

poles, respectively, of a function $F(\lambda)$ inside a closed contour C in λ plane. Using the same hopping integrals $\gamma = \gamma_j$ for the s-SWNTs, Eq. (37) is written as

$$w_\mu = \frac{1}{2\pi i} \oint_{C_1} d\lambda \frac{\partial \log F_\mu(\lambda)}{\partial \lambda}, \quad (40)$$

where C_1 is the unit circle centered at the origin as shown in Fig. 6, $F_\mu(\lambda)$ is given by $\lambda = e^{ik}$ in Eq. (38) divided by the constant γ ,

$$F_\mu(\lambda) = 1 + e^{-i\frac{2\pi}{d}p\mu}\lambda^{\frac{n}{d}} + e^{i\frac{2\pi}{d}q\mu}\lambda^{-\frac{m}{d}}. \quad (41)$$

The right hand side of Eq. (41) is exactly the left hand side of Eq. (23), which has m/d poles at $\lambda = 0$ and, from the analysis in Sec. IV B, N_B roots inside C_1 . Using the argument principle of Eq. (39) to Eq. (40), we have

$$w_\mu = N_B - \frac{m}{d}, \quad (42)$$

which gives the same result with $N_{\text{edge}}^{(L,B)}$ in Eq. (36), showing the bulk-edge correspondence,

$$w_\mu = N_{\text{edge}}^{(L,B)}. \quad (43)$$

Equation (43) shows that the winding number is the number of edge states for B sublattice at left end, which gives more precise relation than other cases which show the relation of winding number and the difference of number of edge states between two sublattices.^{56–58}

It would be worthful to mention the case of zigzag-left handedness, $m > n \geq 0$. For this case, the number of edge states are given by,

$$N_{\text{edge}}^{(L,A)} = N_A - \frac{n}{d}, \quad N_{\text{edge}}^{(L,B)} = 0, \quad (44)$$

since the number of boundary conditions is larger or equal to that of the relevant modes for B sublattice. Using the relation, $N_B - m/d = -(N_A - n/d)$, which holds at $\varepsilon = 0$ since $n_A = 1 - n_B$ (see Table II), regardless of left and right handedness, we get the following bulk-edge correspondence for zigzag-left handedness,

$$w_\mu = -N_{\text{edge}}^{(L,A)}. \quad (45)$$

We now get the bulk-edge correspondence for both zigzag-right and left handedness cases. When sign of

the winding number is positive (negative), the number of edge states for B (A) sublattice is given by the absolute value of the winding number, while that of A (B) sublattice is zero. The bulk-edge correspondence and the number of edge states for A and B sublattices are summarized in Table IV.

TABLE IV. Bulk-edge correspondence and number of edge states for A and B sublattices for the minimal boundary condition.

	Zigzag-right handedness	Zigzag-left handedness
	$n > m \geq 0$	$m > n \geq 0$
w_μ	$N_{\text{edge}}^{(L,B)}$	$-N_{\text{edge}}^{(L,A)}$
$N_{\text{edge}}^{(L,A)}$	0	$N_A - \frac{n}{d}$
$N_{\text{edge}}^{(L,B)}$	$N_B - \frac{m}{d}$	0

In general, the number of edge states depends on the boundary shape. For the case that the termination of A sublattice is at $\ell = \Delta\ell$ and that at B sublattice is at $\ell = 1$, for instance, the winding number which gives the number of edge states should be calculated for the different bulk Hamiltonian as follows (the transformation of the Hamiltonian from H_μ to H'_μ is depicted in Fig. 8);

$$H'_\mu = \sum_{\ell} \sum_{j=1}^3 \gamma_j e^{i\frac{2\pi}{d}\Delta\nu'_j\mu} c_{A(\mu,\ell)}^\dagger c'_{B(\mu,\ell+\Delta\ell'_j+\Delta\ell)} + \text{H.c.} \quad (46)$$

The winding number for Eq. (46) is then calculated as,

$$\begin{aligned} w'_\mu &= \frac{1}{2\pi} \int_0^{2\pi} dk \frac{\partial \arg f'_\mu(k)}{\partial k} \\ &= w_\mu + \Delta\ell, \end{aligned} \quad (47)$$

where

$$f_\mu(k)' = \langle Ak\mu | H'_\mu | Bk\mu \rangle = e^{ik\Delta\ell} f_\mu(k). \quad (48)$$

Note that both Eqs. (19) and (46) gives the same energy band and the same number of evanescent modes for the same chirality (n, m) , since their difference appears only on the phase of off-diagonal term of the Hamiltonian matrix. The number of boundary conditions for the A sublattice increases by $\Delta\ell$ while that for the B sublattice decreases by $\Delta\ell$. Therefore, it can be checked that the number of edge states is given by Eq. (47). Equation (47) explains the numerically observed difference of the numbers of edge states between different boundaries shown in Figs. 2 and 3 in our previous study.²² Note that Eq. (37) itself can be applied to evaluate the number of edge states for m-SWNTs with appropriate values of γ_j to reproduce the narrow gap induced by the curvature and the spin-orbit interaction.²⁰ It is shown in the Appendix C that w_μ can be non-zero values, except for the armchair nanotubes, by employing an analysis with viewpoint of the symmetry of SWNTs.

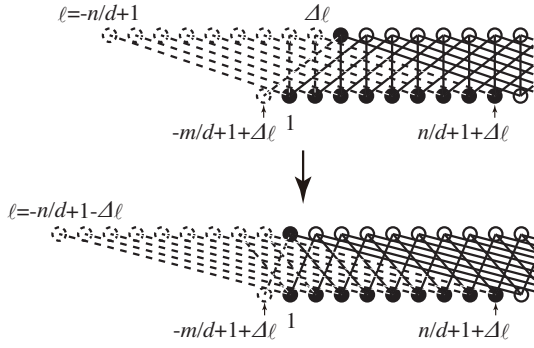


FIG. 8. Transformation of effective 1D lattice model $H_\mu \rightarrow H'_\mu$ to calculate winding number for number of edge states for $(n/d, m/d) = (7, 3)$ and $\Delta\ell = 2$.

Finally, we comment on the applicability of the simplified 1D model. Perturbations could modified the edge states quantitatively. For the metallic SWNTs with narrow energy gap, some edge states could exist in the energy band region because of the effect of the hopping to next nearest neighbor and farther sites.⁴² Breaking of the C_d rotational symmetry also affects as a perturbation to the edge states, which mixes the edge states with different angular momenta. Even though such perturbations changes the energies of edge states, the number of edge states could keeps from the unperturbed case as long as keeping finite energy gap, as shown in Fig. 8 in Ref. 22.

V. CONCLUSION

In summary, we studied the angular momentum of two valleys in the s-SWNTs. The classification of the s-SWNTs in the sense of the angular momentum of valley was given by the integer d . For the case of $d \geq 4$, the two valleys are decoupled in the finite-length nanotubes which keep C_d rotational symmetry. Lift of the fourfold degeneracy is caused by the spin-orbit interaction. On the other hand, for the cases of $d = 1$ and $d = 2$, the coupling of two valleys lifts the fourfold degeneracy. Especially, when $|n - m| = 2$, near the armchair chirality, they are strongly coupled and the effect of the spin-orbit interaction is hidden by the large lift of the degeneracy by valley coupling. The effective 1D lattice model was introduced by extracting relevant angular momentum states, which explained the valley coupling in the eigenfunctions. The analysis on the winding number provided the bulk-edge correspondence for the edge states in the s-SWNTs.

The presented study showed that the valley coupling in the eigenstates and the edge states in the semiconducting energy gap strongly depends on the chirality and boundary shape. The valley coupling occurs in the majority of both metallic and semiconducting SWNTs, even they are defect free and they have clean edges which conserve the angular momentum of bulk states. The recent progress on the separation⁵⁹ and synthesis⁶⁰ of single-

chirality SWNTs, or simultaneous measurement of quantum transport, chirality and the boundary shape by high resolution measurements in atomic scale such as the scanning tunneling spectroscopy^{61,62} or high-resolution Raman spectroscopy⁶³ would enable to observe the chirality and boundary dependences of the valley coupling and the edge states.³⁹⁻⁴¹

ACKNOWLEDGMENTS

We acknowledge JSPS KAKENHI Grants (No. 15K05118 for W. I., No. 25286005 for R. S.), and MEXT KAKENHI Grants (No. 25107001 and No. 25107005 for R. O. and R. S.), Japan. A. Y. is grateful to S. Kobayashi for fruitful discussion.

Appendix A: Discrete energy levels for finite-length valley decoupled s-SWNTs

In Fig. 9, we show numerical calculation of the discrete energy levels for (8, 4) nanotube, which has $d = 4$, as an example for the case of $d \geq 4$. The calculation is done by the same method with Figs. 4 and 3, the extended tight-binding method, for the finite-length of 50.07 nm, with a minimal boundary for both ends which keep the bulk $C_{d=4}$ rotational symmetry. The calculated energy levels show fourfold degeneracy. This clearly shows the decoupling of two valley. In the actual situation, the spin-orbit interaction lifts the fourfold degeneracy.

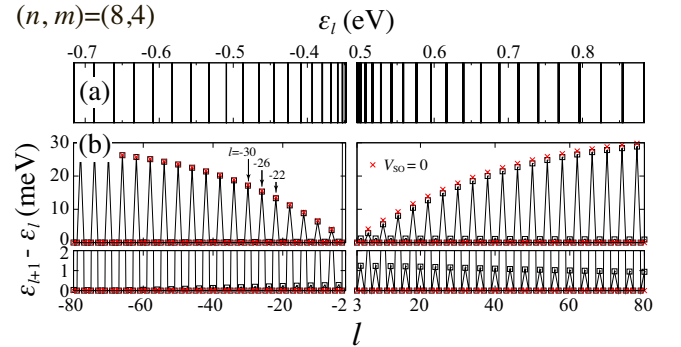


FIG. 9. (Color online) Energy levels for (8, 4) nanotube of 50.07 nm length. (a) Energy levels ϵ_l from valence ($\epsilon_l \leq -0.348$ eV, $l \leq -2$) and conduction ($\epsilon_l \geq 0.496$ eV, $l \geq 3$) bands, where l is the level index. There are also energy levels at $\epsilon_l = 0$ at $l = -1, 0, 1, 2$, which are localized at the ends (not shown). (b) Level separation $\epsilon_{l+1} - \epsilon_l$ as a function of level index l .

Appendix B: Analysis of effective 1D lattice model

Here we give the detailed calculation for Secs. IV B and IV C.

1. Number of evanescent modes

First, we give the detailed derivation of Eq. (24). In the low energy limit $|\varepsilon/\gamma| \ll 1$ and by using the same hopping integrals $\gamma = \gamma_j$, we get the following equations for the A and B modes, respectively, from Eqs. (22) and (23),

$$e^{-i\frac{2\pi}{d}\mu} \lambda'^{\frac{n}{d}} = (-1 - \lambda')^{\frac{n}{d} + \frac{m}{d}}, \quad (\text{B1})$$

$$e^{i\frac{2\pi}{d}\mu} \lambda'^{\frac{m}{d}} = (-1 - \lambda')^{\frac{n}{d} + \frac{m}{d}}. \quad (\text{B2})$$

where

$$\lambda' = e^{-i\frac{2\pi(p+q)\mu}{d}} \lambda^{\frac{n}{d} + \frac{m}{d}} \quad (\text{B3})$$

is introduced since this conversion aligns the evanescent modes of $|\lambda| < 1$, which also satisfy $|\lambda'| < 1$, on a curve between $\lambda'_+ = e^{i2\pi/3}$ and $\lambda'_- = e^{i4\pi/3}$, as shown in Fig. 10. Hereafter we explicitly show the analysis for A mode. Eq. (B1) can be separated into two equations for absolute and phase values as follows;

$$|\lambda'|^{\frac{n}{d}} = |1 + \lambda'|^{\frac{n}{d} + \frac{m}{d}}, \quad (\text{B4})$$

$$\left(\frac{n}{d} + \frac{m}{d}\right) \arg(-1 - \lambda') - \frac{n}{d} \arg \lambda' + \frac{2\pi}{d} \mu = 2\pi l', \quad (\text{B5})$$

where l' is an arbitrary integer. Since Eqs. (B4) and (B5) have the same forms with the equations discussed for the metallic condition,³⁶ the similar discussion can be employed for counting the evanescent modes, as shown below.

The condition (B4) gives a closed curve passing λ'_+ and λ'_- in the complex plane, as shown by the blue curve in Fig. 10. Then, $n/d + m/d$ positions satisfying Eq. (B5) on the curve give the solutions of λ' of Eq. (B1), as shown by the open marks on the blue curve in Fig. 10. The number of evanescent modes at the left end, which satisfy $|\lambda| < 1$, is given by counting the number of modes on the curve in between λ'_+ and λ'_- . The left hand side of Eq. (B5) monotonically decreases when λ' moves from λ'_+ and λ'_- on the curve, since $\arg(-1 - \lambda')$ decreases when $\arg(\lambda')$ increases. Note that $\arg(\lambda'_-)$ and $\arg(-1 - \lambda')$ are defined in $0 \leq \arg(\lambda'_-)$, $\arg(-1 - \lambda') < 2\pi$ for this case. The values of l' satisfying Eq. (B5) at λ'_+ and λ'_- are given by

$$l'_+ = \frac{n+2m}{3d} + \frac{\mu}{d}, \quad l'_- = -\frac{n-m}{3d} + \frac{\mu}{d}, \quad (\text{B6})$$

respectively. Note that l'_\pm are fractional numbers, unlike the metallic case.³⁶ By counting the integers l' in $l'_- < l' < l'_+$ for the cases of $\text{mod}(n/d + m/d, 3) = 1, 2$ for $0 \leq \mu/d < 1/3$, $1/3 < \mu/d < 2/3$, $2/3 < \mu/d < 1$, we get N_A . By employing the similar discussion with above, we also get N_B . The results are summarized in Eq. (24) and in Table II.

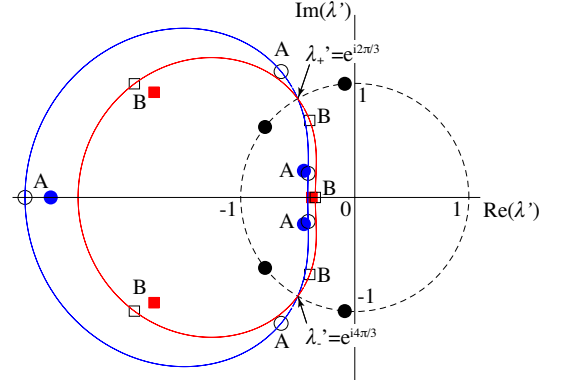


FIG. 10. (Color online) Solutions λ' for Eqs. (22) and (23) in the complex plane for $(n, m) = (6, 4)$, $(d = 2, \text{type-1})$ $\mu = 1$, $p = 2$, $q = 1$. The marks show the solutions at $\varepsilon = 0$ and $|\varepsilon/\gamma| = 0.4$. The same symbols with Fig. 6 are used. Closed blue and red curves give the condition of Eq. (B4) for A mode and the corresponding one for B mode, respectively, and open marks on the curves are the solutions at $\varepsilon = 0$.

2. Evanescent modes and traveling modes

Here we will give the evanescent modes with the longest decay length at $\varepsilon = 0$, Eq. (26), and their changing to traveling modes in Eq. (28) when energy increases or decreases to $|\varepsilon| > \varepsilon_{\text{gap}}/2$. We restrict $d = 1$ and $d = 2$ cases, in which (λ^*, η^*) is also a set of solution for a solution (λ, η) since γ_j , ε and $e^{-i\frac{2\pi}{d}\Delta\nu'_j\mu}$ ($j = 1, 2, 3$) are real numbers.

First, we mention the relation between λ and λ' , which is defined by Eq. (B3), for the mode of $\lambda = \lambda_\tau = e^{i\tau k_1}$. After some algebraic calculation, we get the corresponding phase of $\lambda = \lambda_\tau$ in λ' as follows;

$$\begin{aligned} \arg \lambda'|_{\lambda=\lambda_\tau} &= \tau k_1 \left(\frac{n}{d} + \frac{m}{d}\right) - \frac{2\pi(p+q)\mu}{d} \\ &= \tau \left(\frac{2\pi}{3} + \delta\theta\right) + 2\pi\alpha, \end{aligned} \quad (\text{B7})$$

for both $d = 1$ and $\mu = 1$ of $d = 2$ cases, where α is an integer, and

$$\delta\theta = -t_y \frac{2\pi}{3} \frac{n-m}{2(n^2 + m^2 + nm)}, \quad (\text{B8})$$

where

$$t_y = \begin{cases} +1 & \text{for type-1,} \\ -1 & \text{for type-2,} \end{cases} \quad (\text{B9})$$

is introduced for type-1 [$\text{mod}(2n+m, 3) = 1$] and type-2 [$\text{mod}(2n+m, 3) = 2$] s-SWNTs. Since Eq. (B8) is the small correction, the solution near λ'_+ (λ'_-) corresponds that at K (K') valley.

The evanescent modes with the longest decay length at $\varepsilon = 0$ have λ' closest to λ'_τ , and they are expressed by

$$\lambda' = (1 - \delta r) \exp \left[i\tau \left(\frac{2\pi}{3} + \delta\varphi \right) \right], \quad (\text{B10})$$

with small values of $|\delta r| \ll 1$ and $|\delta \varphi| \ll 1$. For small δr and $\delta \varphi$, we have the relation, $-1 - \lambda' = (1 - \delta r')e^{-i\tau(2\pi/3 - \delta \varphi')}$, where $\delta r' = \delta r/2 + \sqrt{3}\delta \varphi/2$ and $\delta \varphi' = -\sqrt{3}\delta r/2 + \delta \varphi/2$. Eq. (B4) gives the following relation,

$$(n - m)\delta r = \sqrt{3}(n + m)\delta \varphi, \quad (\text{B11})$$

and Eq. (B5) gives the following relation,

$$\frac{\sqrt{3}}{2}(n + m)\delta r + \frac{1}{2}(n - m)\delta \varphi = 2\pi\tau(l'_\tau - l'_{0,\tau})d, \quad (\text{B12})$$

where $l'_{0,\tau}$ is the integer closest to l'_τ . By doing the similar analysis with that after Eq. (B6) in Appendix B1, we get

$$\tau(l'_\tau - l'_{0,\tau})d = -t_y \frac{1}{3}. \quad (\text{B13})$$

From Eqs. (B11) and (B12), we get

$$\delta r = -t_y \frac{2a_z}{3d_t} \left(\frac{n}{d} + \frac{m}{d} \right), \quad \delta \varphi = -t_y \frac{2\pi}{3} \frac{n - m}{2(n^2 + m^2 + nm)}. \quad (\text{B14})$$

In fact, $\delta \varphi = \delta \theta$. The similar calculation for the B mode gives the results which has opposite sign for δr , $-t_y \rightarrow t_y$ in Eq. (B14) while the same equation holds for $\delta \varphi$. The conversion from λ' to λ for Eq. (B10) is performed by using Eqs. (B3) and (B7), then we get

$$\lambda_{\tau,0}^\sigma = \exp \left(i\tau k_1 + t_y \sigma \frac{2a_z}{3d_t} \right), \quad (\text{B15})$$

where $\sigma = 1$ ($\sigma = -1$) for A (B) mode. For the evanescent modes at the left end, which satisfy $|\lambda| < 1$, we get Eq. (26). Substituting $\lambda_{\tau,0}^{\sigma=1}$ of Eq. (B15) for Eq. (22) with $\varepsilon = 0$ and expanding in the first order of a_z/d_t , we get the following relation,

$$1 + e^{i\frac{2\pi}{d}p\mu} e^{-i\tau k_1 \frac{a}{d}} + e^{-i\frac{2\pi}{d}q\mu} e^{i\tau k_1 \frac{a}{d}} = t_y e^{-i[-\frac{2\pi}{d}p\mu + \tau(k_1 \frac{a}{d} + \theta)]} \frac{a}{\sqrt{3}d_t}, \quad (\text{B16})$$

which will be used in the following analysis, where $\theta = \arccos \frac{2n+m}{2\sqrt{n^2+m^2+nm}}$ is the chiral angle.

The evanescent modes in the energy gap are expressed by

$$\lambda_{\tau\kappa} = \exp(i\tau k_1 - \kappa), \quad (\text{B17})$$

where $|\kappa| \leq 2a_z/3d_t$. Substituting Eq. (B17) for Eqs. (22) and (23), expanding in the first order of κ , and using Eq. (B16), we get the energy

$$\varepsilon_\kappa^b = b|\gamma| \frac{\sqrt{3}a}{2a_z} \sqrt{\left(\frac{2a_z}{3d_t} \right)^2 - \kappa^2}, \quad (\text{B18})$$

and η ,

$$\eta_{\tau\kappa}^b = b \exp \left\{ -i \left[-\frac{2\pi}{d}p\mu + \tau \left(k_1 \frac{n}{d} + \theta \right) \right] \right\} \text{sgn}(\gamma) \times t_y \sqrt{\frac{\frac{2a_z}{3d_t} + t_y \kappa}{\frac{2a_z}{3d_t} - t_y \kappa}} \quad (\text{B19})$$

For a state in $|\varepsilon| \geq \varepsilon_{\text{gap}}/2$, the λ solution of Eqs. (22) and (23) has the following form,

$$\lambda_{\tau rk} = \exp[i(\tau k_1 + rk)]. \quad (\text{B20})$$

By the similar calculation with that for Eq. (B18), we get the energy

$$\varepsilon_k^b = b|\gamma| \frac{\sqrt{3}a}{2a_z} \sqrt{k^2 + \left(\frac{2a_z}{3d_t} \right)^2}, \quad (\text{B21})$$

and η ,

$$\eta_{\tau rk}^b = \exp(i\Phi_{\tau rk}^b), \quad (\text{B22})$$

where

$$\Phi_{\tau rk}^b = \frac{2\pi}{d}p\mu - \tau \left(k_1 \frac{n}{d} + \theta \right) + \arg \left[b\gamma \left(t_y \frac{2a_z}{3d_t} - irk \right) \right]. \quad (\text{B23})$$

3. Strong coupling of two valleys

The wavefunctions of A and B sublattices above and below the energy gap near the left end are written as

$$\phi_{A\kappa}^b(\ell) = \sum_{\tau} g_{A\tau\kappa}^b \lambda_{\tau}^{\ell} + \sum_{m_A=1}^{N_A} c_{Am_A} (\lambda_{Am_A}^<)^\ell, \quad (\text{B24})$$

$$\phi_{B\kappa}^b(\ell) = \sum_{\tau} g_{B\tau\kappa}^b \lambda_{\tau}^{\ell} + \sum_{m_B=1}^{N_B} c_{Bm_B} (\lambda_{Bm_B}^<)^\ell. \quad (\text{B25})$$

The envelope functions $g_{\sigma\tau\kappa}^b$ are regarded as constant values near the left end. The boundary conditions of Eqs. (32) and (33) for the wavefunctions of Eqs. (B24) and (B25) are expressed by the following matrix form,

$$D_o \mathbf{c}_o = 0, \quad (\text{B26})$$

where

$$D_o = \begin{pmatrix} A_+ & A_- & 0 & 0 & D_A & 0 \\ 0 & 0 & B_+ & B_- & 0 & D_B \end{pmatrix}, \quad (\text{B27})$$

with the submatrices,

$$A_\tau = \begin{pmatrix} 1 \\ (\lambda_\tau)^{-1} \\ \vdots \\ (\lambda_\tau)^{-\frac{n}{d}+1} \end{pmatrix}, \quad B_\tau = \begin{pmatrix} 1 \\ (\lambda_\tau)^{-1} \\ \vdots \\ (\lambda_\tau)^{-\frac{m}{d}+1} \end{pmatrix}, \quad (\text{B28})$$

$$D_A = \begin{pmatrix} 1 & \cdots & 1 \\ (\lambda_{A1}^<)^{-1} & \cdots & (\lambda_{AN_A}^<)^{-1} \\ \vdots & \ddots & \vdots \\ (\lambda_{A1}^<)^{-\frac{n}{d}+1} & \cdots & (\lambda_{AN_A}^<)^{-\frac{n}{d}+1} \end{pmatrix}, \quad (\text{B29})$$

$$D_B = \begin{pmatrix} 1 & \cdots & 1 \\ (\lambda_{B1}^<)^{-1} & \cdots & (\lambda_{BN_B}^<)^{-1} \\ \vdots & \ddots & \vdots \\ (\lambda_{B1}^<)^{-\frac{m}{d}+1} & \cdots & (\lambda_{BN_B}^<)^{-\frac{m}{d}+1} \end{pmatrix}, \quad (\text{B30})$$

and

$$\mathbf{c}_o^T = (g_{A+,k}^b, g_{A-,k}^b, g_{B+,k}^b, g_{B-,k}^b, c_{A1}, \dots, c_{AN_A}, c_{B1}, \dots, c_{BN_B}). \quad (\text{B31})$$

In general, we have the following relation between two complex numbers,

$$g_{B\tau k}^b = r_\tau g_{A\tau k}^b e^{i\Phi_\tau}, \quad (\text{B32})$$

where $r_\tau \geq 0$, $0 \leq \Phi_\tau < 2\pi$. Using Eq. (B32), Eq. (B26) is rewritten as

$$D\mathbf{c} = 0, \quad (\text{B33})$$

where

$$D = \begin{pmatrix} A_+ & A_- & D_A & 0 \\ r_+ e^{i\Phi_+} B_+ & r_- e^{i\Phi_-} B_- & 0 & D_B \end{pmatrix}, \quad (\text{B34})$$

and

$$\mathbf{c}^T = (g_{A+,k}^b, g_{A-,k}^b, c_{A1}, \dots, c_{A\frac{n}{d}-1}, c_{B1}, \dots, c_{B\frac{m}{d}-1}). \quad (\text{B35})$$

The matrix D is the $(n/d + m/d) \times (n/d + m/d)$ square matrix.

Hereafter let us focus on the case of $m = n - 2$, in which $N_A = n/d - 1$ and $N_B = m/d - 1$. Since the number of boundary conditions is one less than that of the relevant modes for both A and B sublattice, both A and B sublattices have non-trivial solutions, $g_{\sigma\tau k}^b \neq 0$ for both $\sigma = A$ and B . For this case, r_+ and r_- are finite positive values ($r_\tau > 0$). To satisfy Eq. (B33) for non-trivial coefficients, $\mathbf{c} \neq 0$, the determinant of the matrix D should be zero, $|D| = 0$. We will show the condition for $|D| = 0$.

Before the evaluation of $|D|$, we will show some relations, which will be used later. By using the roots of the left hand side of Eq. (22), it is rewritten as,

$$\begin{aligned} & 1 + e^{i\frac{2\pi}{d}p\mu} \lambda^{-\frac{n}{d}} + e^{-i\frac{2\pi}{d}q\mu} \lambda^{\frac{m}{d}} \\ &= \frac{e^{-i\frac{2\pi}{d}q\mu}}{\lambda^{\frac{n}{d}}} \left[\lambda^{\frac{n}{d} + \frac{m}{d}} + e^{i\frac{2\pi}{d}q\mu} \lambda^{\frac{n}{d}} + e^{i\frac{2\pi}{d}(p+q)\mu} \right] \\ &= \frac{e^{-i\frac{2\pi}{d}q\mu}}{\lambda^{\frac{n}{d}}} \prod_{m_1=1}^{\frac{n}{d}-1} (\lambda - \lambda_{Am_1}^<) \\ &\quad \times \prod_{m_2=1}^{\frac{m}{d}-1} (\lambda - \lambda_{Am_2}^>) \prod_{\tau=\pm} (\lambda - \lambda_{\tau,0}) \\ &= \frac{e^{-i\frac{2\pi}{d}q\mu}}{\lambda} \prod_{m_1=1}^{\frac{n}{d}-1} (-\lambda_{Am_1}^<) \prod_{m_1=1}^{\frac{n}{d}-1} \left(\frac{1}{\lambda} - \frac{1}{\lambda_{Am_1}^<} \right) \\ &\quad \times \prod_{m_2=1}^{\frac{m}{d}-1} (\lambda - \lambda_{Am_2}^>) \prod_{\tau=\pm} (\lambda - \lambda_{\tau,0}). \end{aligned} \quad (\text{B36})$$

The value $\prod_{m_1=1}^{\frac{n}{d}-1} (-\lambda_{Am_1}^<)$ in the right hand side of Eq. (B36) is a real number. This is because there is another root, $\lambda_{Am_1}^{<*}$, for a complex root $\lambda_{Am_1}^<$, for $d = 1$ and $d = 2$ since $e^{i\frac{2\pi}{d}q\mu}$ and $e^{i\frac{2\pi}{d}(p+q)\mu}$, which appear in the left hand side of Eq. (B36), are real numbers. For the traveling mode $(\lambda, \eta) = (\lambda_{\tau rk}, \eta_{\tau rk}^b)$, a part of right hand side of (B36) is calculated as,

$$\frac{1}{\lambda_{\tau rk}} \prod_{\tau=\pm} (\lambda_{\tau rk} - \lambda_{\tau,0}) = - \left(t_y \frac{2a_z}{3d_t} - irk \right) 2i\tau \sin k_1. \quad (\text{B37})$$

Therefore, we have the following relation,

$$\begin{aligned} & \prod_{m_1=1}^{\frac{n}{d}-1} \left(\frac{1}{\lambda_{\tau rk}} - \frac{1}{\lambda_{Am_1}^<} \right) \prod_{m_2=1}^{\frac{m}{d}-1} (\lambda_{\tau rk} - \lambda_{Am_2}^>) \\ &= R e^{i\frac{2\pi}{d}\Delta\nu_3\mu} e^{i(\frac{\pi}{2} + \Phi_{\tau rk}^b)} \end{aligned} \quad (\text{B38})$$

where R is a finite real number, which does not depend on τ , r , k and b . Further, the evanescent modes of B sublattice, $\lambda_{Bm_B}^<$ in (B30), are replaced by the evanescent modes of A sublattice at the right end, $\lambda_{Am_A}^>$, which satisfy $|\lambda_{Am_A}^>| > 1$, that is,

$$\lambda_{Bm'}^< = \frac{1}{\lambda_{Am'}^>}, \quad (\text{B39})$$

for $m' = 1, \dots, N_B$, because there is one-to-one correspondence between the evanescent mode of B sublattice at the left end and that of A sublattice at the right end, since $(1/\lambda^*, 1/\eta^*)$ is the conjugated mode of (λ, η) for Eqs. (22) and (23), and, there is another root, $\lambda_{Am_1}^{<*}$, for a complex root $\lambda_{Am_1}^<$ for $d = 1$ and $d = 2$, as mentioned before.

The determinant of D is expanded as,

$$|D| = r_+ e^{i\Phi_+} |A_- D_A| |B_+ D_B| - r_- e^{i\Phi_-} |A_+ D_A| |B_- D_B|. \quad (\text{B40})$$

By using Eq. (B39), and the relation on the Vander-

monde matrix, the determinant is calculated to be,

$$|D| = (-1)^{\frac{n(n-1)}{2} + \frac{m(m-1)}{2}} \prod_{1 \leq m_1 < m_2 \leq \frac{n}{d}-1} \left(\frac{1}{\lambda_{Am_1}^<} - \frac{1}{\lambda_{Am_2}^<} \right) \prod_{1 \leq m_1 < m_2 \leq \frac{m}{d}-1} (\lambda_{Am_1}^> - \lambda_{Am_2}^>) \\ \times \left\{ r_+ e^{i\Phi_+} \prod_{m_1=1}^{\frac{n}{d}-1} \left(\frac{1}{\lambda_-} - \frac{1}{\lambda_{Am_1}^<} \right) \prod_{m_2=1}^{\frac{m}{d}-1} (\lambda_- - \lambda_{Am_2}^>) - r_- e^{-i\Phi_-} \prod_{m_1=1}^{\frac{n}{d}-1} \left(\frac{1}{\lambda_+} - \frac{1}{\lambda_{Am_1}^<} \right) \prod_{m_2=1}^{\frac{m}{d}-1} (\lambda_+ - \lambda_{Am_2}^>) \right\}. \quad (\text{B41})$$

Using Eq. (B38), we have

$$|D| \propto e^{i(\Phi_+ + \Phi_{\tau=-1, r, k=0}^b)} + r_- e^{i(\Phi_- + \Phi_{\tau=1, r, k=0}^b)}. \quad (\text{B42})$$

Therefore, the condition of $|D| = 0$ is expressed by the following relations,

$$r_+ = r_-, \quad (\text{B43})$$

and

$$\Phi_+ - \Phi_- = \Phi_{\tau=1, r, k=0}^b - \Phi_{\tau=-1, r, k=0}^b + \pi + 2\pi\alpha, \quad (\text{B44})$$

where α is an arbitrary integer.

In fact, the envelope functions are constructed from the leftgoing and rightgoing modes as expressed in Eq. (30), that is,

$$g_{A\tau k}^b = c_{A\tau rk} + c_{A\tau -rk}, \quad (\text{B45})$$

$$g_{B\tau k}^b = e^{i\Phi_{\tau rk}^b} \left[c_{A\tau rk} + e^{i(\Phi_{\tau -rk}^b - \Phi_{\tau rk}^b)} c_{A\tau -rk} \right], \quad (\text{B46})$$

By converting Eqs. (B45) and (B46) into the form of Eq (B32), we can check the explicit form of the envelope functions which satisfy Eqs. (B43) and (B44).

Let us consider the following two cases, (i) near the top of the valence band and bottom of the conduction band, $k \ll a_z/d_t$, and, (ii) the linear dispersion region, $k \gg a_z/d_t$. For the case of (i), since $\Phi_{\tau -rk}^b \simeq \Phi_{\tau rk}^b$, from Eqs. (B45) and (B46) we have

$$g_{B\tau k}^b = e^{i\Phi_{\tau rk=0}^b} g_{A\tau k}^b. \quad (\text{B47})$$

By comparing Eqs. (B32) and (B47), we have $r_\tau = 1$ and $\Phi_\tau = \Phi_{\tau rk=0}^b$. For this case Eq. (B44) cannot be satisfied, that is, $|D| \neq 0$. Therefore, $c = 0$, to satisfy the boundary conditions. This means that the following relation holds,

$$g_{\sigma\tau k}^b \propto \sin(k\ell) \quad (\text{B48})$$

for the envelope functions of both $\sigma = A$ and $\sigma = B$. Similar to the case of $m \neq n-2$, the boundary conditions are satisfied by constructing the eigenstate in each valley separately. Therefore, two valleys are decoupled and the valley degeneracy occurs.

For the case of (ii) the linear dispersion region, in which the relation $|\Phi_{\tau rk}^b - \Phi_{\tau -rk}^b| = \pi$ holds, Eq. (B46) is rewritten as

$$g_{B\tau k}^b = e^{i\Phi_{\tau rk}^b} (c_{A\tau rk} - c_{A\tau -rk}). \quad (\text{B49})$$

To satisfy Eq. (B44), we have

$$c_{A\tau rk}^b \neq 0, \text{ and } c_{A, \tau, -r, k}^b = 0, \quad (\text{B50})$$

for either $r = 1$ or $r = -1$, or,

$$\arg(c_{A\tau rk}^b) - \arg(c_{A\tau -rk}^b) = \pi\alpha, \quad (\text{B51})$$

where α is an arbitrary integer.

When we apply the boundary conditions for the right end, the second condition of Eq. (B51) is too strict to determine quantized wavenumber. For $d = 1$ and $d = 2$ cases, the following relation on the wavefunctions reflecting the parity symmetry of the effective 1D Hamiltonian, which corresponds to the C_2' rotational symmetry around the axis perpendicular to the nanotube axis, is utilized for the boundary conditions of the right end;²²

$$\phi_{Ak}^b(\ell) = p_a \phi_{Bk}^b(N_s + 1 - \ell) \text{ for any } \ell, \quad (\text{B52})$$

where $p_a = \pm 1$ are the parity eigenvalues, $\ell = N_s$ is the right end. Equation (B52) is calculated as,

$$c_{\sigma\tau k}^b = p_a e^{i\Phi_{\tau -rk}^b} e^{-i(k_1 + rk)(N_s + 1)} c_{\sigma - \tau - rk}^b, \quad (\text{B53})$$

For the case of Eq. (B51), Eq. (B53) is applied for both $r = 1$ and $r = -1$. This is overcomplete to determine the quantized wavenumber. Therefore, the condition of Eq. (B50), which means the strong valley coupling, is realized for the finite-length systems.

4. Edge states at zero energy

By employing the similar discussion with Appendix B3, we will show the condition of emerging of edge states.

For long nanotubes, the eigenfunctions within the energy gap, $|\varepsilon| < \varepsilon_{\text{gap}}/2$, are written as,

$$\phi_A(\ell) = \sum_{m_A=1}^{N_A} c_{Am_A} (\lambda_{Am_A}^<)^\ell + \sum_{m_B=1}^{N_B} c_{Bm_B} \frac{1}{\eta_{Bm_B}} (\lambda_{Bm_B}^<)^\ell, \quad (\text{B54})$$

$$\phi_B(\ell) = \sum_{m_A=1}^{N_A} c_{Am_A} \eta_{Am_A} (\lambda_{Am_A}^<)^\ell + \sum_{m_B=1}^{N_B} c_{Bm_B} (\lambda_{Bm_B}^<)^\ell, \quad (\text{B55})$$

where $|\eta_{Am_A}| < 1$ and $|1/\eta_{Bm_B}| < 1$, and especially, $\eta_{Am_A} = 1/\eta_{Bm_B} = 0$ at $\varepsilon = 0$. By employing the boundary conditions of Eqs. (32) and (33) to the eigenfunctions (B54) and (B55), we get the following relation,

$$D_e \mathbf{c}_e = 0, \quad (\text{B56})$$

where

$$D_e = \begin{pmatrix} D_A & E_B \\ E_A & D_B \end{pmatrix}, \quad (\text{B57})$$

and

$$\mathbf{c}_e^T = (c_{A1}, \dots, c_{AN_A}, c_{B1}, \dots, c_{BN_B}), \quad (\text{B58})$$

where D_A and D_B are given in Eqs. (B29) and (B30), and

$$E_A = \begin{pmatrix} \eta_{A1} & \dots & \eta_{AN_A} \\ \eta_{A1} (\lambda_{A1}^<)^{-1} & \dots & \eta_{AN_A} (\lambda_{AN_A}^<)^{-1} \\ \vdots & \ddots & \vdots \\ \eta_{A1} (\lambda_{A1}^<)^{-\frac{n}{d}+1} & \dots & \eta_{AN_A} (\lambda_{AN_A}^<)^{-\frac{n}{d}+1} \end{pmatrix}, \quad (\text{B59})$$

$$E_B = \begin{pmatrix} \frac{1}{\eta_{B1}} & \dots & \frac{1}{\eta_{BN_B}} \\ \frac{1}{\eta_{B1}} (\lambda_{B1}^<)^{-1} & \dots & \frac{1}{\eta_{BN_B}} (\lambda_{BN_B}^<)^{-1} \\ \vdots & \ddots & \vdots \\ \frac{1}{\eta_{B1}} (\lambda_{B1}^<)^{-\frac{m}{d}+1} & \dots & \frac{1}{\eta_{BN_B}} (\lambda_{BN_B}^<)^{-\frac{m}{d}+1} \end{pmatrix}, \quad (\text{B60})$$

The condition that Eq. (B56) has non-trivial solutions, $\mathbf{c}_e \neq 0$, is the determinant of the matrix D_e is zero, $|D_e| = 0$. This condition is satisfied when $\eta_{Am_A} = 1/\eta_{Bm_B} = 0$, which is the case of $\varepsilon = 0$, since $E_A = 0$ and $E_B = 0$, and both D_A and D_B are not square matrices. At finite energy $\varepsilon \neq 0$, η_{Am_A} and η_{Bm_B} have finite values, then the determinant cannot be zero, $|D_e| \neq 0$, except for accidental cases.

Appendix C: Winding number under symmetry of SWNTs

It is convenient to consider topological invariants in each subspace of the Hilbert space under a symmetry.⁶⁴

The topological property of the subsystem H_μ is characterized by the winding number w_μ defined by,^{44,45}

$$w_\mu = \frac{i}{4\pi} \int_0^{2\pi} dk \text{Tr} \left\{ \Gamma_\mu(k) [H_\mu(k)]^{-1} \frac{\partial H_\mu(k)}{\partial k} \right\}, \quad (\text{C1})$$

where

$$H_\mu(k) = \begin{pmatrix} 0 & f_\mu(k) \\ f_\mu(k)^* & 0 \end{pmatrix} \quad (\text{C2})$$

is the 2×2 Hamiltonian matrix formed by the base of Bloch functions $|\sigma k \mu\rangle$ with $\sigma = A$ and B , and

$$\Gamma_\mu(k) = \begin{pmatrix} 1 & 0 \\ 0 & -1 \end{pmatrix} \quad (\text{C3})$$

is known as so-called the chiral operator which multiple -1 on $|Bk\mu\rangle$ in the operated state. Since w_μ can be either positive or negative integers, the number of total edge states at each end and each spin is given by $\sum_\mu |w_\mu|$. We put μ and k on the operator $\Gamma_\mu(k)$, to emphasize that the operation acts in (k, μ) subspace of the Hilbert space. The above defined winding number is a topological invariant since the bipartite system H_μ , as well as the superconductors within the mean field theory, satisfies so-called sublattice (or chiral) symmetry, $\{\Gamma_\mu(k), H_\mu(k)\} = 0$.

The winding number corresponds to the number of edge states on an end in which A and B sublattices are terminated at the same position. [As examples, see left ends in Figs. 5 (a) and 5 (b)]. In other words, for a case that A and B sublattices are terminated at different positions in the original 1D model, a modified model, in which translation of B sublattice is performed for the original model so as to have an end terminating both sublattices at the same position, should be employed for calculating the winding number. In general, the numbers of edge states for the different terminations are different each other, such as the minimal and orthogonal boundaries discussed in Ref. 22 for the same bulk systems. Substituting Eqs. (C2) and (C3) for Eq. (C1), one gets Eq. (37) which is convenient to evaluate the winding number numerically. Since $f_\mu(k)$ is a periodic function of k of period 2π , the winding number is an integer. Hereafter we will show the winding number is a nontrivial value, that is, w_μ can be non-zero, under the symmetry of SWNTs. In the following, we employ a generalized discussion for application to not only the SWNTs but also other materials. The following discussion is restricted for the spinless case.

For the time reversal operation, \mathcal{T} , which changes (k, μ) to $(-k, -\mu)$, we have

$$\mathcal{T} H_\mu(k) \mathcal{T}^{-1} = H_{-\mu}(-k) \quad (\text{C4})$$

and

$$\mathcal{T} \Gamma_\mu(k) \mathcal{T}^{-1} = p_t \Gamma_{-\mu}(-k). \quad (\text{C5})$$

where $p_t = 1$ for the SWNTs. When the operation also changes the “pseudo-spin” σ to $-\sigma$, Eq. (C5) shows anticommutation relation of $p_t = -1$, which occurs for so-called class DIII and CI superconductors in which the Nambu pseudo-spin for the BCS particle-hole index changes the sign under the \mathcal{T} operation.^{47–49} Using Eqs. (C4) and (C5) to Eq. (C1), it is shown that the winding number of $-\mu$ subspace, $w_{-\mu}$, has the following relation,

$$w_{-\mu} = p_t w_\mu, \quad (\text{C6})$$

where we used the relation of $\langle \beta | O | \alpha \rangle = \langle \tilde{\alpha} | \mathcal{T} O^\dagger \mathcal{T}^{-1} | \tilde{\beta} \rangle$ for the antilinear operator \mathcal{T} and the anticommutation relation of $\Gamma_\mu(k)$ and $H_\mu(k)$, where O is a linear operator and tilde on the states indicates the antilinear operated states, $|\tilde{\alpha}\rangle = \mathcal{T}|\alpha\rangle$ and $|\tilde{\beta}\rangle = \mathcal{T}|\beta\rangle$.⁶⁵

In the sense of symmetry of point group, chiral SWNTs contains C'_2 rotational symmetry around the axis perpendicular to the nanotube axis, in addition to C_d rotational symmetry. The C'_2 operation changes (k, μ) to $(-k, -\mu)$, and the sublattice index σ to $-\sigma$, where $-\sigma = \text{B (A)}$ for $\sigma = \text{A (B)}$. We have the relations

$$C'_2 H_\mu(k) C'^{-1}_2 = H_{-\mu}(-k) \quad (\text{C7})$$

and

$$C'_2 \Gamma_\mu(k) C'^{-1}_2 = p_2 \Gamma_{-\mu}(-k), \quad (\text{C8})$$

where $p_2 = -1$. The anticommutation relation of Eq. (C8) reflects that C'_2 exchanges the A and B sublattices. Then, we have the following relation for the winding number,

$$w_{-\mu} = -p_2 w_\mu. \quad (\text{C9})$$

Since Eqs. (C6) and (C9) are identical for the present case, which do not give extra restriction for the winding number, it is concluded that w_μ can be a non-zero value. For a case of $p_2 = 1$ reflecting the “pseudo-spin” keeping C'_2 operation, for instance, gives the opposite result that $w_\mu = 0$, even though this is not the present case.

For the achiral SWNTs, the armchair and the zigzag nanotubes, there exist extra symmetries. Let us consider mirror reflection σ_v with a vertical mirror plane including the nanotube axis, which changes μ to $-\mu$ while the direction of k is kept unchanged. Strictly speaking, σ_v changes (k, μ) to $(k', -\mu)$ where $k' = k - 2\Delta\theta\mu$ has the additional constant to k reflecting that \mathbf{Q}_1/d , which separates the two neighbor cutting lines, has $-\Delta\theta/2\pi$ components in \mathbf{Q}_2 direction in the oblique coordinates for (k, μ) (see Sec. II A.) Further, σ_v exchanges the sublattice index $\text{A} \leftrightarrow \text{B}$ for the armchair nanotubes while it is unchanged for the zigzag nanotubes. We have the relations

$$\sigma_v H_\mu(k) \sigma_v^{-1} = H_{-\mu}(k') \quad (\text{C10})$$

and

$$\sigma_v \Gamma_\mu(k) \sigma_v^{-1} = p_v \Gamma_{-\mu}(k'), \quad (\text{C11})$$

where $p_v = -1$ (1) for the armchair (zigzag) nanotubes. Using Eqs. (C10) and (C11) to (C1), we have the following relation,

$$w_{-\mu} = p_v w_\mu, \quad (\text{C12})$$

The relation (C12), combined with Eq. (C6), gives $w_\mu = 0$ for the armchair nanotubes while it does not give extra restriction for the zigzag nanotubes. For the other symmetry, mirror symmetry with a plane perpendicular to the nanotube axis, σ_h , we have $\sigma_h \Gamma_\mu(k) \sigma_h^{-1} = p_h \Gamma_\mu(-k')$, where $p_h = 1$ (-1) for the armchair (zigzag) nanotubes. The similar calculation with above gives

$$w_\mu = -p_h w_\mu, \quad (\text{C13})$$

which accidentally gives the same results from Eqs. (C9) and (C12). The inversion symmetry does not give any further extra restrictions from above since the operation is represented by the combination of C'_2 and σ_v operations.

To complete the symmetric property of the winding number, we also add the property from the d -fold rotational symmetry, which requires $[C_d, H_\mu(k)] = 0$. From the relation $C_d \Gamma_\mu C_d^{-1} = p_d \Gamma_\mu$, where $p_d = 1$ for the SWNTs, and Eq. (C1), we have

$$w_\mu = p_d w_\mu. \quad (\text{C14})$$

This is nontrivial, however for the other case of $p_d = -1$ where the d -fold rotation exchanges the A and B sublattices, we have the winding number $w_\mu = 0$.

The obtained necessary conditions for the nontrivial winding numbers are summarized as,

$$p_d = -p_2 = p_v = -p_h = 1, \quad (p_t = 1), \quad (\text{C15})$$

for the SWNTs and other bipartite insulators,

$$p_d = p_2 = -p_v = -p_h = 1, \quad (p_t = -1), \quad (\text{C16})$$

for the topological superconductors.⁶⁶

As mentioned above, the SWNTs, except for the armchair nanotubes, have nontrivial winding number. Here the indices of the SWNTs are summarized as follows;

$$p_t = 1, \text{ and, } p_d = -p_2 = 1, \quad (\text{C17})$$

for the all SWNTs. In addition to Eq. (C17),

$$p_v = -p_h = 1, \quad (\text{C18})$$

for the zigzag nanotubes, and

$$p_v = -p_h = -1, \quad (\text{C19})$$

for the armchair nanotubes. As another example of the application of Eq. (C15), we employ it to so-called the Su-Schrieffer-Heeger model for the polyacetylene.⁶⁷ The system has no rotational symmetry ($d = 1$), $p_2 = -1$, $p_v = 1$ and $p_t = 1$ are all the relevant indices for the

system, then the system has nontrivial winding number, which is consistent with the well-known properties of zero-energy edge states for the Su-Schrieffer-Heeger model.^{68,69}

The result that there is no edge states for the armchair nanotubes from the above discussion is consistent with the numerical calculation in Ref. 22 which does not show any evanescent modes for the armchair nanotube with the minimal boundary. Note that the small energy gap of the order of sub-milli-electron-volt is induced by

the spin-orbit interaction.²⁰ This property for the armchair nanotubes is contrast to the other topological materials,^{70–72} in which edge states appears in the energy gap induced by the spin-orbit interaction. We confirmed by the extended tight-binding calculation with large spin-orbit interaction ($V_{\text{SO}} = 1$ eV) for $(n, m) = (6, 6)$, 50 nm length armchair nanotube that there is no edge state in the energy gap of ~ 0.13 eV. The effective 1D model with additional imaginary hopping terms,¹⁶ to reproduces the spin-orbit effect, also showed winding number being zero for the armchair nanotubes.

-
- * izumida@cmpt.phys.tohoku.ac.jp
† okuyama@flex.phys.tohoku.ac.jp
‡ ai@rover.nuap.nagoya-u.ac.jp
- ¹ E. A. Laird, F. Kuemmeth, G. A. Steele, K. Grove-Rasmussen, J. Nygård, K. Flensberg, and L. P. Kouwenhoven, “Quantum transport in carbon nanotubes,” *Rev. Mod. Phys.* **87**, 703 (2015).
 - ² W. Liang, M. Bockrath, and H. Park, “Shell filling and exchange coupling in metallic single-walled carbon nanotubes,” *Phys. Rev. Lett.* **88**, 126801 (2002).
 - ³ D. H. Cobden and J. Nygård, “Shell filling in closed single-wall carbon nanotube quantum dots,” *Phys. Rev. Lett.* **89**, 046803 (2002).
 - ⁴ P. Jarillo-Herrero, J. Kong, H. S. J. van der Zant, C. Dekker, L. P. Kouwenhoven, and S. De Franceschi, “Electronic transport spectroscopy of carbon nanotubes in a magnetic field,” *Phys. Rev. Lett.* **94**, 156802 (2005).
 - ⁵ S. Moriyama, T. Fuse, M. Suzuki, Y. Aoyagi, and K. Ishibashi, “Four-electron shell structures and an interacting two-electron system in carbon-nanotube quantum dots,” *Phys. Rev. Lett.* **94**, 186806 (2005).
 - ⁶ S. Sapmaz, P. Jarillo-Herrero, J. Kong, C. Dekker, L. P. Kouwenhoven, and H. S. J. van der Zant, “Electronic excitation spectrum of metallic carbon nanotubes,” *Phys. Rev. B* **71**, 153402 (2005).
 - ⁷ H. Maki, Y. Ishiwata, M. Suzuki, and K. Ishibashi, “Electronic transport of a carbon nanotube quantum dot in different coupling regimes,” *Jpn. J. Appl. Phys.* **44**, 4269 (2005).
 - ⁸ J. Cao, Q. Wang, and H. Dai, “Electron transport in very clean, as-grown suspended carbon nanotubes,” *Nat. Mater.* **4**, 745 (2005).
 - ⁹ A. Makarovski, L. An, J. Liu, and G. Finkelstein, “Persistent orbital degeneracy in carbon nanotubes,” *Phys. Rev. B* **74**, 155431 (2006).
 - ¹⁰ S. Moriyama, T. Fuse, and K. Ishibashi, “Shell structures and electron-spin configurations in single-walled carbon nanotube quantum dots,” *Phys. Stat. Sol. B* **244**, 2371 (2007).
 - ¹¹ J. V. Holm, H. I. Jørgensen, K. Grove-Rasmussen, J. Paaske, K. Flensberg, and P. E. Lindelof, “Gate-dependent tunneling-induced level shifts observed in carbon nanotube quantum dots,” *Phys. Rev. B* **77**, 161406(R) (2008).
 - ¹² F. Kuemmeth, S. Ilani, D. C. Ralph, and P. L. McEuen, “Coupling of spin and orbital motion of electrons in carbon nanotubes,” *Nature* **452**, 448 (2008).
 - ¹³ S. H. Jhang, M. Marganska, Y. Skourski, D. Preusche, B. Witkamp, M. Grifoni, H. van der Zant, J. Wosnitza, and C. Strunk, “Spin-orbit interaction in chiral carbon nanotubes probed in pulsed magnetic fields,” *Phys. Rev. B* **82**, 041404(R) (2010).
 - ¹⁴ T. S. Jespersen, K. Grove-Rasmussen, J. Paaske, K. Muraki, T. Fujisawa, J. Nygård, and K. Flensberg, “Gate-dependent spin-orbit coupling in multielectron carbon nanotubes,” *Nat. Phys.* **7**, 348 (2011).
 - ¹⁵ G. A. Steele, F. Pei, E. A. Laird, J. M. Jol, H. B. Meerwaldt, and L. P. Kouwenhoven, “Large spin-orbit coupling in carbon nanotubes,” *Nat. Commun.* **4**, 1573 (2013).
 - ¹⁶ T. Ando, “Spin-orbit interaction in carbon nanotubes,” *J. Phys. Soc. Jpn.* **69**, 1757 (2000).
 - ¹⁷ L. Chico, M. P. Lopez-Sancho, and M. C. Munoz, “Spin splitting induced by spin-orbit interaction in chiral nanotubes,” *Phys. Rev. Lett.* **93**, 176402 (2004).
 - ¹⁸ D. Huertas-Hernando, F. Guinea, and A. Brataas, “Spin-orbit coupling in curved graphene, fullerenes, nanotubes, and nanotube caps,” *Phys. Rev. B* **74**, 155426 (2006).
 - ¹⁹ L. Chico, M. P. López-Sancho, and M. C. Muñoz, “Curvature-induced anisotropic spin-orbit splitting in carbon nanotubes,” *Phys. Rev. B* **79**, 235423 (2009).
 - ²⁰ W. Izumida, K. Sato, and R. Saito, “Spin-orbit interaction in single wall carbon nanotubes: Symmetry adapted tight-binding calculation and effective model analysis,” *J. Phys. Soc. Jpn.* **78**, 074707 (2009).
 - ²¹ J.-S. Jeong and H.-W. Lee, “Curvature-enhanced spin-orbit coupling in a carbon nanotube,” *Phys. Rev. B* **80**, 075409 (2009).
 - ²² W. Izumida, R. Okuyama, and R. Saito, “Valley coupling in finite-length metallic single-wall carbon nanotubes,” *Phys. Rev. B* **91**, 235442 (2015).
 - ²³ M. Marganska, P. Chudzinski, and M. Grifoni, “The two classes of low-energy spectra in finite carbon nanotubes,” *Phys. Rev. B* **92**, 075433 (2015).
 - ²⁴ A. M. Lunde, K. Flensberg, and A.-P. Jauho, “Intershell resistance in multiwall carbon nanotubes: A Coulomb drag study,” *Phys. Rev. B* **71**, 125408 (2005).
 - ²⁵ D. R. Schmid, S. Smirnov, M. Margańska, A. Dirnauchner, P. L. Stiller, M. Grifoni, A. K. Hüttel, and C. Strunk, “Broken SU(4) symmetry in a Kondo-correlated carbon nanotube,” *Phys. Rev. B* **91**, 155435 (2015).
 - ²⁶ M. Ferrier, T. Arakawa, T. Hata, R. Fujiwara, R. Delagrè, R. Weil, R. Deblock, R. Sakano, A. Oguri, and K. Kobayashi, “Universality of non-equilibrium fluctuations in strongly correlated quantum liquids,”

- Nat Phys **12**, 230–235 (2016).
- 27 P. Jarillo-Herrero, S. Sapmaz, C. Dekker, L. P. Kouwenhoven, and H. S. J. van der Zant, “Electron-hole symmetry in a semiconducting carbon nanotube quantum dot,” *Nature* **429**, 389 (2004).
 - 28 V. V. Deshpande and M. Bockrath, “The one-dimensional Wigner crystal in carbon nanotubes,” *Nat. Phys.* **4**, 314 (2008).
 - 29 R. Saito, G. Dresselhaus, and M. S. Dresselhaus, *Physical Properties of Carbon Nanotubes* (Imperial College Press, London, 1998).
 - 30 Ge. G. Samsonidze, R. Saito, A. Jorio, M. A. Pimenta, A. G. Souza Filho, A. Grüneis, G. Dresselhaus, and M. S. Dresselhaus, “The concept of cutting lines in carbon nanotube science,” *J. Nanosci. Nanotechnol.* **3**, 431–458 (2003).
 - 31 E. B. Barros, A. Jorio, G. G. Samsonidze, R. B. Capaz, A. G. Souza Filho, J. M. Filho, G. Dresselhaus, and M. S. Dresselhaus, “Review on the symmetry-related properties of carbon nanotubes,” *Phys. Rep.* **431**, 261 (2006).
 - 32 Ge. G. Samsonidze, A. Grüneis, R. Saito, A. Jorio, A. G. Souza Filho, G. Dresselhaus, and M. S. Dresselhaus, “Interband optical transitions in left- and right-handed single-wall carbon nanotubes,” *Phys. Rev. B* **69**, 205402 (2004).
 - 33 C. T. White, D. H. Robertson, and J. W. Mintmire, “Helical and rotational symmetries of nanoscale graphitic tubules,” *Phys. Rev. B* **47**, 5485 (1993).
 - 34 R. A. Jishi, M. S. Dresselhaus, and G. Dresselhaus, “Symmetry properties of chiral carbon nanotubes,” *Phys. Rev. B* **47**, 16671 (1993).
 - 35 A. Jorio, C. Fantini, M. A. Pimenta, R. B. Capaz, Ge. G. Samsonidze, G. Dresselhaus, M. S. Dresselhaus, J. Jiang, N. Kobayashi, A. Grüneis, and R. Saito, “Resonance Raman spectroscopy (n, m)-dependent effects in small-diameter single-wall carbon nanotubes,” *Phys. Rev. B* **71**, 075401 (2005).
 - 36 A. R. Akhmerov and C. W. J. Beenakker, “Boundary conditions for Dirac fermions on a terminated honeycomb lattice,” *Phys. Rev. B* **77**, 085423 (2008).
 - 37 D. Porezag, Th. Frauenheim, Th. Köhler, G. Seifert, and R. Kaschner, “Construction of tight-binding-like potentials on the basis of density-functional theory: Application to carbon,” *Phys. Rev. B* **51**, 12947 (1995).
 - 38 M. Fujita, K. Wakabayashi, K. Nakada, and K. Kusakabe, “Peculiar localized state at zigzag graphite edge,” *J. Phys. Soc. Jpn.* **65**, 1920 (1996).
 - 39 Z. Klusek, Z. Waqar, E. A. Denisov, T. N. Kompaniets, I. V. Makarenko, A. N. Titkov, and A. S. Bhatti, “Observations of local electron states on the edges of the circular pits on hydrogen-etched graphite surface by scanning tunneling spectroscopy,” *Appl. Surf. Sci.* **161**, 508 (2000).
 - 40 Y. Kobayashi, K.-I. Fukui, T. Enoki, K. Kusakabe, and Y. Kaburagi, “Observation of zigzag and armchair edges of graphite using scanning tunneling microscopy and spectroscopy,” *Phys. Rev. B* **71**, 193406 (2005).
 - 41 Y. Niimi, T. Matsui, H. Kambara, K. Tagami, M. Tsukada, and Hiroshi Fukuyama, “Scanning tunneling microscopy and spectroscopy of the electronic local density of states of graphite surfaces near monoatomic step edges,” *Phys. Rev. B* **73**, 085421 (2006).
 - 42 K. Sasaki, S. Murakami, and R. Saito, “Stabilization mechanism of edge states in graphene,” *Appl. Phys. Lett.* **88**, 13110 (2006).
 - 43 W. Izumida, A. Vikström, and R. Saito, “Asymmetric velocities of Dirac particles and vernier spectrum in metallic single-wall carbon nanotubes,” *Phys. Rev. B* **85**, 165430 (2012).
 - 44 X.G. Wen and A. Zee, “Winding number, family index theorem, and electron hopping in a magnetic field,” *Nucl. Phys. B* **316**, 641 (1989).
 - 45 S. Ryu and Y. Hatsugai, “Topological origin of zero-energy edge states in particle-hole symmetric systems,” *Phys. Rev. Lett.* **89**, 077002 (2002).
 - 46 K. Sasaki, S. Murakami, R. Saito, and Y. Kawazoe, “Controlling edge states of zigzag carbon nanotubes by the Aharonov-Bohm flux,” *Phys. Rev. B* **71**, 195401 (2005).
 - 47 A. P. Schnyder, S. Ryu, A. Furusaki, and A. W. W. Ludwig, “Classification of topological insulators and superconductors in three spatial dimensions,” *Phys. Rev. B* **78**, 195125 (2008).
 - 48 A. Kitaev, “Periodic table for topological insulators and superconductors,” *AIP Conf. Proc.* **1134**, 22 (2009).
 - 49 S. Ryu, A. P. Schnyder, A. Furusaki, and A. W. W. Ludwig, “Topological insulators and superconductors: tenfold way and dimensional hierarchy,” *New J. Phys.* **12**, 065010 (2010).
 - 50 D. J. Thouless, M. Kohmoto, M. P. Nightingale, and M. den Nijs, “Quantized Hall conductance in a two-dimensional periodic potential,” *Phys. Rev. Lett.* **49**, 405 (1982).
 - 51 M. Kohmoto, “Topological invariant and the quantization of the Hall conductance,” *Ann. Phys.* **160**, 343 (1985).
 - 52 R. B. Laughlin, “Quantized Hall conductivity in two dimensions,” *Phys. Rev. B* **23**, 5632–5633 (1981).
 - 53 B. I. Halperin, “Quantized Hall conductance, current-carrying edge states, and the existence of extended states in a two-dimensional disordered potential,” *Phys. Rev. B* **25**, 2185 (1982).
 - 54 Y. Hatsugai, “Edge states in the integer quantum Hall effect and the Riemann surface of the Bloch function,” *Phys. Rev. B* **48**, 11851 (1993).
 - 55 Y. Hatsugai, “Chern number and edge states in the integer quantum Hall effect,” *Phys. Rev. Lett.* **71**, 3697 (1993).
 - 56 V. Gurarie, “Single-particle Green’s functions and interacting topological insulators,” *Phys. Rev. B* **83**, 085426 (2011).
 - 57 M. Sato, Y. Tanaka, K. Yada, and T. Yokoyama, “Topology of Andreev bound states with flat dispersion,” *Phys. Rev. B* **83**, 224511 (2011).
 - 58 A. M. Essin and V. Gurarie, “Bulk-boundary correspondence of topological insulators from their respective Green’s functions,” *Phys. Rev. B* **84**, 125132 (2011).
 - 59 H. Liu, D. Nishide, T. Tanaka, and H. Kataura, “Large-scale single-chirality separation of single-wall carbon nanotubes by simple gel chromatography,” *Nat Commun* **2**, 309 (2011).
 - 60 J. R. Sanchez-Valencia, T. Dienel, O. Groning, I. Shorubalko, A. Mueller, M. Jansen, K. Amsharov, P. Ruffieux, and R. Fasel, “Controlled synthesis of single-chirality carbon nanotubes,” *Nature* **512**, 61 (2014).
 - 61 J. W. G. Wildöer, L. C. Venema, A. G. Rinzler, R. E. Smalley, and C. Dekker, “Electronic structure of atomically resolved carbon nanotubes,” *Nature* **391**, 59 (1998).
 - 62 T. W. Odom, J.-L. Huang, P. Kim, and C. M. Lieber, “Atomic structure and electronic properties of single-walled carbon nanotubes,” *Nature* **391**, 62 (1998).
 - 63 A. Hartschuh, E. J. Sánchez, X. S. Xie, and L. Novotny, “High-resolution near-field raman

- microscopy of single-walled carbon nanotubes,” Phys. Rev. Lett. **90**, 095503 (2003).
- ⁶⁴ M. Koshino, T. Morimoto, and M. Sato, “Topological zero modes and Dirac points protected by spatial symmetry and chiral symmetry,” Phys. Rev. B **90**, 115207 (2014).
- ⁶⁵ J. J. Sakurai and J. J. Napolitano, *Modern Quantum Mechanics (Second Edition)* (Addison-Wesley, San Francisco, 2010).
- ⁶⁶ A. Yamakage *et. al.*, in preparation,.
- ⁶⁷ W. P. Su, J. R. Schrieffer, and A. J. Heeger, “Solitons in polyacetylene,” Phys. Rev. Lett. **42**, 1698 (1979).
- ⁶⁸ M. Z. Hasan and C. L. Kane, “*Colloquium* : Topological insulators,” Rev. Mod. Phys. **82**, 3045 (2010).
- ⁶⁹ X.-L. Qi and S.-C. Zhang, “Topological insulators and superconductors,” Rev. Mod. Phys. **83**, 1057 (2011).
- ⁷⁰ C. L. Kane and E. J. Mele, “Quantum spin Hall effect in graphene,” Phys. Rev. Lett. **95**, 226801 (2005).
- ⁷¹ Y. Kim, B. J. Wieder, C. L. Kane, and A. M. Rappe, “Dirac line nodes in inversion-symmetric crystals,” Phys. Rev. Lett. **115**, 036806 (2015).
- ⁷² A. Yamakage, Y. Yamakawa, Y. Tanaka, and Y. Okamoto, “Line-node Dirac semimetal and topological insulating phase in noncentrosymmetric pnictides CaAgX ($X = \text{P, As}$),” J. Phys. Soc. Jpn. **85**, 013708 (2016).